The Astronomical Journal, 164:70 (34pp), 2022 August https://doi.org/10.3847/1538-3881/ac73ff

The TESS Grand Unified Hot Jupiter Survey. I. Ten TESS Planets

Samuel W. Yee[1], Joshua N. Winn[1], Joel D. Hartman[1], Joseph E. Rodriguez[2], George Zhou[3], Samuel N. Quinn[4], David W. Latham[4], Allyson Bieryla[4], Karen A. Collins[4], Brett C. Addison[3], Isabel Angelo[5], Khalid Barkaoui[6,7,8], Paul Benni[9], Andrew W. Boyle[10], Rafael Brahm[11,12], R. Paul Butler[13], David R. Ciardi[10], Kevin I. Collins[14], Dennis M. Conti[15], Jeffrey D. Crane[13], Fei Dai[16], Courtney D. Dressing[17], Jason D. Eastman[4], Zahra Essack[7,18], Raquel Forés-Toribio[19,20], Elise Furlan[10], Tianjun Gan[21], Steven Giacalone[17], Holden Gill[17], Eric Girardin[22], Thomas Henning[23], Christopher E. Henze[24], Melissa J. Hobson[23], Jonathan Horner[3], Andrew W. Howard[25], Steve B. Howell[24], Chelsea X. Huang[3], Howard Isaacson[3,17], Jon M. Jenkins[24], Eric L. N. Jensen[26], Andrés Jordán[11,12], Stephen R. Kane[27], John F. Kielkopf[28], Slawomir Lasota[29], Alan M. Levine[18], Jack Lubin[30], Andrew W. Mann[31], Bob Massey[32], Kim K. McLeod[33], Matthew W. Mengel[3], Jose A. Muñoz[19,20], Felipe Murgas[8,34], Enric Palle[8,34], Peter Plavchan[35], Adam Popowicz[29], Don J. Radford[36], George R. Ricker[18], Pamela Rowden[37], Boris S. Safonov[38], Arjun B. Savel[39], Richard P. Schwarz[40], S. Seager[7,18,41], Ramotholo Sefako[42], Avi Shporer[18], Gregor Srdoc[43], Ivan S. Strakhov[38], Johanna K. Teske[13], C. G. Tinney[44], Dakotah Tyler[5], Robert A. Wittenmyer[3], Hui Zhang[45], and Carl Ziegler[46]

[1] Department of Astrophysical Sciences, Princeton University, 4 Ivy Lane, Princeton, NJ 08544, USA
[2] Department of Physics and Astronomy, Michigan State University, East Lansing, MI 48824, USA
[3] University of Southern Queensland, Centre for Astrophysics, West Street, Toowoomba, QLD 4350, Australia
[4] Center for Astrophysics | Harvard & Smithsonian, 60 Garden Street, Cambridge, MA 02138, USA
[5] Department of Physics & Astronomy, University of California Los Angeles, Los Angeles, CA 90095, USA
[6] Astrobiology Research Unit, Université de Liège, 19C Allée du 6 Août, B-4000 Liège, Belgium
[7] Department of Earth, Atmospheric and Planetary Sciences, Massachusetts Institute of Technology, Cambridge, MA 02139, USA
[8] Instituto de Astrofísica de Canarias (IAC), E-38205 La Laguna, Tenerife, Spain
[9] Acton Sky Portal (Private Observatory), Acton, MA, USA
[10] Caltech/IPAC-NASA Exoplanet Science Institute, 770 S. Wilson Avenue, Pasadena, CA 91106, USA
[11] Facultad de Ingeniería y Ciencias, Universidad Adolfo Ibaáñez, Av. Diagonal las Torres 2640, Penñalolén, Santiago, Chile
[12] Millennium Institute for Astrophysics, Chile
[13] Earth and Planets Laboratory, Carnegie Institution for Science, 5241 Broad Branch Road, NW, Washington, DC 20015, USA
[14] George Mason University, 4400 University Drive, Fairfax, VA, 22030 USA
[15] American Association of Variable Star Observers, 49 Bay State Road, Cambridge, MA 02138, USA
[16] Division of Geological and Planetary Science, California Institute of Technology, Pasadena, CA 91125, USA
[17] Department of Astronomy, University of California Berkeley, Berkeley, CA 94720, USA
[18] Department of Physics and Kavli Institute for Astrophysics and Space Research, Massachusetts Institute of Technology, Cambridge, MA 02139, USA
[19] Departamento de Astronomía y Astrofísica, Universidad de Valencia, E-46100 Burjassot, Valencia, Spain
[20] Observatorio Astronómico, Universidad de Valencia, E-46980 Paterna, Valencia, Spain
[21] Department of Astronomy, Tsinghua University, Beijing 100084, People's Republic of China
[22] Grand Pra Observatory, Switzerland
[23] Max-Planck-Institut fur Astronomie, Konigstuhl 17, D-69117 Heidelberg, Germany
[24] NASA Ames Research Center, Moffett Field, CA 94035, USA
[25] Department of Astronomy, California Institute of Technology, Pasadena, CA 91125, USA
[26] Department of Physics & Astronomy, Swarthmore College, Swarthmore, PA 19081, USA
[27] Department of Earth and Planetary Sciences, University of California, Riverside, CA 92521, USA
[28] Department of Physics and Astronomy, University of Louisville, Louisville, KY 40292, USA
[29] Silesian University of Technology, Department of Electronics, Electrical Engineering and Microelectronics, Akademicka 16, 44-100 Gliwice, Poland
[30] Department of Physics & Astronomy, University of California, Irvine, Irvine, CA 92697, USA
[31] Department of Physics and Astronomy, The University of North Carolina at Chapel Hill, Chapel Hill, NC 27599-3255, USA
[32] Villa '39 Observatory, Landers, CA 92285, USA
[33] Department of Astronomy, Wellesley College, Wellesley, MA 02481, USA
[34] Departamento de Astrofísica, Universidad de La Laguna (ULL), E-38206 La Laguna, Tenerife, Spain
[35] George Mason University, 4400 University Drive MS 3F3, Fairfax, VA 22030, USA
[36] Brierfield Observatory, New South Wales, Australia
[37] Royal Astronomical Society, Burlington House, Piccadilly, London W1J 0BQ, UK
[38] Sternberg Astronomical Institute, Lomonosov Moscow State University, 119992, Universitetskij prospekt 13, Moscow, Russia
[39] Department of Astronomy, University of Maryland, College Park, College Park, MD, USA
[40] Patashnick Voorheesville Observatory, Voorheesville, NY 12186, USA
[41] Department of Aeronautics and Astronautics, MIT, 77 Massachusetts Avenue, Cambridge, MA 02139, USA
[42] South African Astronomical Observatory, P.O. Box 9, Observatory, Cape Town 7935, South Africa
[43] Kotizarovci Observatory, Sarsoni 90, 51216 Viskovo, Croatia
[44] Exoplanetary Science at UNSW, School of Physics, UNSW Sydney, NSW 2052, Australia
[45] Shanghai Astronomical Observatory, Chinese Academy of Sciences, Shanghai 200030, People's Republic of China
[46] Department of Physics, Engineering and Astronomy, Stephen F. Austin State University, 1936 North Street, Nacogdoches, TX 75962, USA
Received 2022 March 23; revised 2022 May 18; accepted 2022 May 21; published 2022 July 27

Abstract

Hot Jupiters—short-period giant planets—were the first extrasolar planets to be discovered, but many questions about their origin remain. NASA's Transiting Exoplanet Survey Satellite (TESS), an all-sky search for transiting planets, presents an opportunity to address these questions by constructing a uniform sample of hot Jupiters for demographic study through new detections and unifying the work of previous ground-based transit surveys. As the first results of an effort to build this large sample of planets, we report here the discovery of 10 new hot Jupiters (TOI-2193A b, TOI-2207b, TOI-2236b, TOI-2421b, TOI-2567b, TOI-2570b, TOI-3331b, TOI-3540A b, TOI-3693b, TOI-4137b). All of the planets were identified as planet candidates based on periodic flux dips observed by TESS, and were subsequently confirmed using ground-based time-series photometry, high-angular-resolution imaging, and high-resolution spectroscopy coordinated with the TESS Follow-up Observing Program. The 10 newly discovered planets orbit relatively bright F and G stars ($G < 12.5$, $T_{\rm eff}$ between 4800 and 6200 K). The planets' orbital periods range from 2 to 10 days, and their masses range from 0.2 to 2.2 Jupiter masses. TOI-2421b is notable for being a Saturn-mass planet and TOI-2567b for being a "sub-Saturn," with masses of 0.322 ± 0.073 and 0.195 ± 0.030 Jupiter masses, respectively. We also measured a detectably eccentric orbit ($e = 0.17 \pm 0.05$) for TOI-2207b, a planet on an 8 day orbit, while placing an upper limit of $e < 0.052$ for TOI-3693b, which has a 9 day orbital period. The 10 planets described here represent an important step toward using TESS to create a large and statistically useful sample of hot Jupiters.

Unified Astronomy Thesaurus concepts: Exoplanets (498); Hot Jupiters (753); Transits (1711); Exoplanet astronomy (486); Exoplanet detection methods (489)

Supporting material: machine-readable tables

1. Introduction

The origin of hot Jupiters is one of the longest-standing unresolved problems in exoplanet science. Prior to the discovery of the first hot Jupiter 51 Pegasi b (Mayor & Queloz 1995), our understanding of planet formation was entirely based on our knowledge of our solar system. It was thought that giant planets could only form beyond a few astronomical units from their host stars, where the surface density of solids within the protoplanetary disk would be high enough to allow for the formation of a solid body massive enough to undergo runaway gas accretion. The existence of hot Jupiters implies that either this expectation was incorrect and giant planets can form close in to their host stars, or that the initially wide orbits of giant planets can sometimes shrink by a factor of 100 (see the reviews by Dawson & Johnson 2018; Fortney et al. 2021, and references therein). In the latter scenario, the orbital shrinkage might be due to gravitational interactions with the gaseous protoplanetary disk, and would therefore need to occur within the first few million years after the formation of the star (Lin & Papaloizou 1986), or the orbital alterations might be caused by eccentricity excitation followed by tidal orbital circularization, which need not occur early in the system's history (Rasio & Ford 1996; Fabrycky & Tremaine 2007). Each of these possible formation pathways would shape the population of hot Jupiters in different ways, and hence studying the demographics of hot Jupiters and the distributions of their orbital properties may help us understand their relative importance.

NASA's ongoing Transiting Exoplanet Survey Satellite (TESS) mission (Ricker et al. 2015) was designed to detect smaller planets—super-Earths and sub-Neptunes—but TESS is also capable of revolutionizing our knowledge of hot Jupiter demographics. As a nearly all-sky space-based photometric survey that dwells on a given star field for 27 days at a time, TESS should be able to identify nearly all of the hot Jupiters that transit stars that are bright and nearby enough for detailed follow-up observations and characterization (Zhou et al. 2019). Simulations have predicted that the TESS planet catalog will eventually contain ≈400 hot Jupiters around FGK stars brighter than $G = 12.5$ (Yee et al. 2021). Such a sample would be an order of magnitude larger than the sample of 40 hot Jupiters found during the original Kepler mission, which is the largest statistically useful sample of such planets currently available. The process of constructing a very large sample of hot Jupiters around bright stars is greatly facilitated and accelerated by the fact that hundreds of these planets have already been discovered by the ground-based transit surveys such as the Trans-Atlantic Exoplanet Survey (TrES; Alonso et al. 2004), XO (McCullough et al. 2005), the Wide Angle Search for Planets (WASP; Pollacco et al. 2006), the Hungarian Automated Telescope Network (HATNet and HATSouth; Bakos et al. 2004, 2013), the Kilodegree Extremely Little Telescope (KELT; Pepper et al. 2007, 2012), and the Next-Generation Transit Survey (NGTS; Wheatley et al. 2018), accounting for roughly 40% of the expected 400 planets in a $G < 12.5$ magnitude-limited sample. The hard work of these previous surveyors over many years led to the discovery of many important and well-studied systems, but the selection functions of these surveys are complex, different from each other, and not well documented. TESS will provide a homogeneous data set that encompasses essentially all of the previously known planets and has a selection function that should be easier to model. Hence, TESS offers the possibility of unifying all of the previous surveys and leveraging over two decades of observational effort.

Still, even with TESS, expanding and completing a statistical sample suitable for demographic study will require a significant follow-up effort to rule out astrophysical false positives (generally eclipsing binaries that masquerade as transiting planets), measure planet masses, and model the selection function. Ground-based imaging and time-series photometric follow-up with higher angular resolution than TESS can be used to check for nearby eclipsing binaries and confirm that the transit signal belongs to the identified star and not a foreground or background star. Additional transit observations help to improve our knowledge of the planet parameters and transit ephemerides, while observations in multiple bandpasses can also be used to check for chromatic effects that are indicative of eclipsing binaries. High-resolution Doppler spectroscopy

provides final confirmation of the planet's existence and measures its mass, as well as providing a high signal-to-noise spectrum that is useful for characterizing the host star.

Given all the different types of observations and resources that are needed, confirming hundreds of new hot Jupiters from TESS within a reasonable amount of time is only feasible with a large community effort.

The lead authors of this paper have begun to organize such an effort, the Grand Unified Hot Jupiter Survey, by playing a linking role between the new planet discoveries from various TESS follow-up groups, and the planets (and false positives) that have already been investigated in previous planet searches. This work is being conducted as part of the TESS Follow-up Observing Program (TFOP; Collins et al. 2018; ExoFOP 2019),[47,48] which provides a platform for coordinating observations and sharing data, and is open to any interested astronomer.

The 10 planets described in this paper are the first newly discovered planets from this survey and are based on data contributed by many TFOP members. The planets are known by their TESS Object of Interest (TOI) numbers: TOI-2193A b, TOI-2207b, TOI-2236b, TOI-2421b, TOI-2567b, TOI-2570b, TOI-3331b, TOI-3540A b, TOI-3693b, and TOI-4137b. Section 2.1 presents time-series photometry from TESS, and Sections 2.2 through 2.4 describe ground-based follow-up photometry, imaging, and spectroscopic follow-up observations. Section 3 presents a characterization of each host star, and Section 4 describes the application of `EXOFASTv2` (Eastman et al. 2019) to jointly model all of the data and determine the parameters of each system. Section 5 examines the properties of the new planets within the context of the entire known sample of hot Jupiters, and Section 6 draws some conclusions.

2. Observations and Data

2.1. TESS Photometry

All of the new planets described here were first detected in TESS photometry. TESS observes a $24^\circ \times 96^\circ$ region of the sky for 27 days at a time, before rotating its field of view to a new sector. During its initial two-year Prime Mission (Sectors 1—26, running from 2018 July to 2020 July), TESS obtained high-precision photometry of $\gtrsim$200,000 preselected stars with a 2 min cadence, with the remainder of the field of view being observed in the full-frame images (FFIs) at 30 minute cadence. With the Extended Mission beginning in 2020 (Sectors 27 onward), 2 min cadence data continues to be obtained for $\approx$20,000 targets per sector, while the FFI cadence has been reduced to 10 minutes.

The 2 min TESS photometry was extracted and reduced by the TESS Science Processing Operations Center (SPOC) pipeline, as described by Jenkins et al. (2016). Only 1 of the 10 planet-hosting stars presented in this paper had been preselected for 2 min cadence observations (TOI-2207, Sector 27). However, several others were added to the short-cadence target list in the Extended Mission following their identification as planet candidates in the FFIs from the Prime Mission. The longer-cadence FFI data were calibrated with the `tica` software (Fausnaugh et al. 2020), and the light curves were extracted with the MIT Quick-Look Pipeline (QLP; Huang et al. 2020a, 2020b; Kunimoto et al. 2021).

Both the SPOC pipeline and QLP search the extracted light curves for transit-like signals ("Threshold Crossing Events" or TCEs), which are then vetted by the TESS Science Office (TSO). Objects with signals surviving the vetting process are designated TESS Objects of Interest (TOIs; Guerrero et al. 2021) and public notifications are distributed. All of the planets in this paper were alerted as TOIs, including some from the recent search of QLP light curves for stars fainter than $T > 10.5$ by Kunimoto et al. (2022). Table 1 summarizes the 10 targets and the TESS sectors they were observed in.

Table 1
Summary of TESS Observations

Target	Sector	Source	Cadence (s)
TOI-2193	13	SPOC	1800
…	27	SPOC	120
TOI-2207	27	SPOC	120
TOI-2236	12,13	SPOC	1800
…	27,39	SPOC	600
TOI-2421	3	SPOC	1800
…	30	SPOC	600
TOI-2567	14–26	SPOC	1800
…	40,41	SPOC	120
TOI-2570	19	SPOC	1800
…	44,45	SPOC	120
TOI-3331	13	QLP	1800
TOI-3540	15	QLP	1800
TOI-3693	17,18	SPOC	1800
TOI-4137	19,26	SPOC	1800

In addition, four of the targets had previously been identified as "community TOIs" (cTOIs) by separate investigators. TOI-2421b was first flagged as a planet candidate by Montalto et al. (2020), who used the DIAmante pipeline to extract difference imaging light curves from the first year of TESS FFIs. They then identified transit events in the light curves with the Box-Least Squares algorithm (Kovács et al. 2002), and vetted the candidate events with a random forest classifier. TOI-2567b, TOI-2570b, and TOI-4137b were identified as planet candidates by Olmschenk et al. (2021), who classified light curves from the SPOC-calibrated FFIs extracted by the `eleanor` pipeline (Feinstein et al. 2019) with a convolutional neural network. These light curves were then subjected to the Quasiperiodic Automated Transit Search (QATS; Carter & Agol 2013; Kruse et al. 2019) pipeline and vetted with the Discovery and Vetting of Exoplanets pipeline (DAVE; Kostov et al. 2019). All four cTOIs were later promoted to TOIs following vetting by the TESS Science Office (Mireles et al. 2021).

We identified these targets as candidate hot Jupiters ($R_p > 8\ R_\oplus$, $P < 10$ days) from the TOI catalog, with selection based on catalog photometry and astrometry indicating that they orbit FGK stars. We then began performing follow-up observations to determine whether the transit-like signals are truly from transiting planets or are instead from eclipsing binaries or other "false positives." When analyzing each planetary system (Section 4), we used all of the available photometry from TESS. We used the `lightkurve` package (Lightkurve Collaboration et al. 2018) to download the TESS light curves from the Mikulski Archive for Space Telescopes (MAST). When available, we used light curves produced from the SPOC

[47] https://heasarc.gsfc.nasa.gov/docs/tess/followup.html
[48] https://exofop.ipac.caltech.edu/tess/

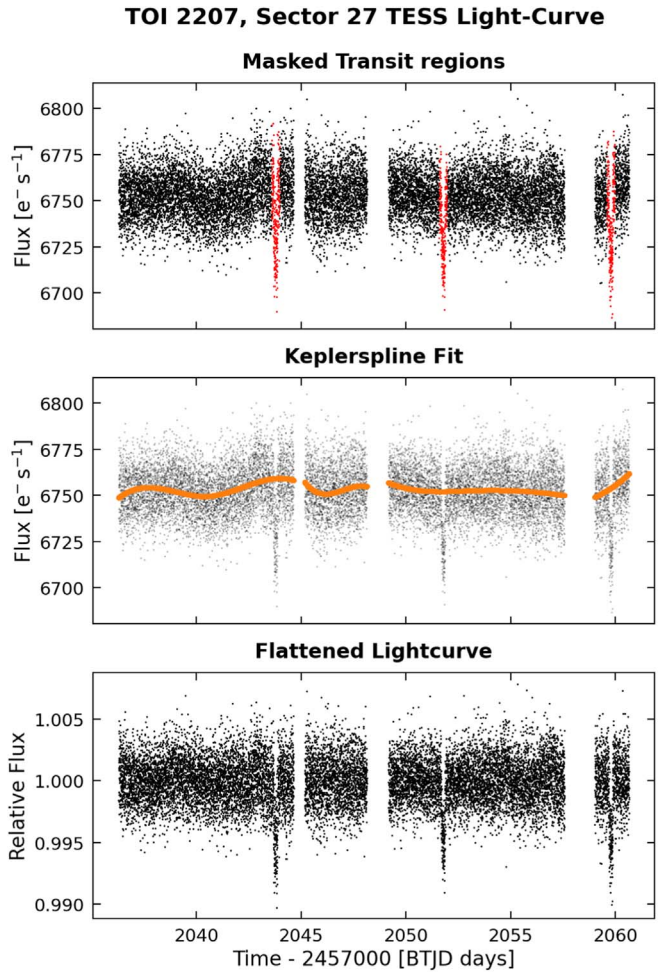

Figure 1. TESS Sector 27 light curve for TOI-2207, extracted by the SPOC pipeline. Top panel: SPOC PDC light curve, with red points highlighting transit events, which are masked out when performing the spline fit. Middle panel: `Keplerspline` fit to the masked light curve. Bottom panel: Flattened light curve.

pipeline—this applies to all the short-cadence data, as well as some of the long-cadence FFI data, for which the SPOC pipeline has recently begun processing 160,000 targets per sector (Caldwell et al. 2020). We used the Presearch Data Conditioning (PDC; Stumpe et al. 2012; Smith et al. 2012; Stumpe et al. 2014) light curves, which have been corrected for instrumental effects. We additionally "flattened" the SPOC PDC light curves with the `Keplerspline`[49] routine (Vanderburg & Johnson 2014; Shallue & Vanderburg 2018), which fits a spline to the light curve (with transit events masked) to correct for stellar or instrumentally induced variability (Figure 1). When SPOC light curves were unavailable for the long-cadence data, we used the light curves extracted by the QLP, which were also flattened with `Keplerspline`. We provide the flattened and normalized TESS photometry in Table 2.

2.2. Ground-based Photometry

Additional ground-based photometry of each of our targets was obtained as part of TFOP's seeing-limited photometry subgroup 1 (SG1). These multiband photometric observations

[49] https://github.com/avanderburg/keplersplinev2

Table 2
Flattened & Normalized TESS Photometry

TOI	Sector	BJD_{TDB}	Flux[a]	Flux Err.
2193	13	2458657.514245	0.999797	0.000731
2193	13	2458657.535079	0.999887	0.000734
2193	13	2458657.555913	1.000377	0.000736
2193	13	2458657.597580	0.996574	0.000740
2193	13	2458657.618414	0.992282	0.000740
2193	13	2458657.680915	1.000831	0.000741

Note.
[a] Flux has been detrended and normalized such that the mean out-of-transit flux has a baseline of 1.0.

(This table is available in its entirety in machine-readable form.)

of individual transits helped to rule out false-positive scenarios such as nearby eclipsing binaries. We also used the ground-based light curves to refine the transit parameters and ephemerides. Observations were obtained from the Brierfield Observatory; KeplerCam on the Fred Lawrence Whipple Observatory (FLWO) 1.2 m telescope; the Hazelwood Observatory; the Acton Sky Portal; the Villa '39 observatory; the Observatori Astronòmic de la Universitat de València (OAUV) TURIA2 0.3 m telescope; the Grand-Pra Observatory; the Silesian University of Technology Observatories (SUTO) OTIVAR 0.3 m telescope; the MEarth-South telescope array (Nutzman & Charbonneau 2008; Berta et al. 2012) at the Cerro Tololo Inter-American Observatory (CTIO); as well as the 0.4 m and 1.0 m telescopes of the Las Cumbres Observatory Global Telescope (LCOGT; Brown et al. 2013) global network, using sites at the Observatorio del Teide, CTIO, the Siding Spring Observatory (SSO), and the South African Astronomical Observatory (SAAO). Data reduction and aperture photometry for all follow-up observations, except for the MEarth-South observations, was done with the `AstroImageJ` software (Collins et al. 2017). The MEarth-South data were reduced according to the procedures described in Berta et al. (2012) and Irwin et al. (2007). We summarize the observations and facilities used for each target in Table 3, and present the complete set of photometric observations in Table 4.

2.3. High-resolution Imaging

We also obtained high-angular-resolution imaging of all of our target systems, in order to detect and characterize stellar companions that might have been blended with the primary target in the TESS images. This allows us to assess the spectroscopic follow-up potential of a target star, eliminate false-positive scenarios, and evaluate the impact of any contamination on the fitted planetary properties. Table 5 summarizes the observations made for each system, which were coordinated by the TFOP high-resolution imaging subgroup 3 (SG3). Nearby companions were detected in three cases : TOI-2193, TOI-3331, and TOI-3540, with imaging shown in Figures 2, 3 and 4, respectively. No companions were found for the other targets down to detection limits, and plots illustrating these observations can be found at the end of this paper, in Figure 13.

TOI-2193, TOI-2207, TOI-2421, TOI-3331, and TOI-3540 were observed in the *I* band with the high-resolution camera (HRCam; Tokovinin & Cantarutti 2008), a speckle imaging

Table 3
Summary of Ground-based Photometric Follow-up Observations

Target	Facility/Instrument	Aperture (m)	Filter	Date (UT)	Cadence (s)	Precision[a] (mmag)	Detrending Vectors
TOI-2193 b	Brierfield	0.36	I	2020 Sep 23	195	4.0	Airmass, Y (T1)
⋯	LCO SAAO/Sinistro	1.0	z'	2020 Sep 27	52	2.5	Width, Total Counts
⋯	LCO SAAO/Sinistro	1.0	i'	2020 Oct 14	52	2.0	Sky/Pixel
⋯	LCO CTIO/Sinistro	1.0	B	2021 Jul 07	100	2.3	Airmass
⋯	LCO SAAO/Sinistro	1.0	B	2021 Jul 07	100	1.2	Airmass
⋯	LCO CTIO/Sinistro	1.0	z'	2021 Jul 26	110	1.3	Width
TOI-2207 b	CTIO/MEarth-South	0.4	I	2021 Jun 14	50	3.7	FWHM, SKY, Meridian Flip
⋯	LCO CTIO/Sinistro	1.0	z'	2021 Jun 21	90	1.2	FWHM, Total Counts
TOI-2236 b	Brierfield	0.36	I	2020 Oct 05	195	3.0	Airmass
⋯	LCO CTIO/Sinistro	1.0	B	2021 Jun 27	166	2.6	None
⋯	LCO CTIO/Sinistro	1.0	z'	2021 Jun 27	166	3.1	Total Counts, FWHM
TOI-2421 b	LCO SAAO/Sinistro	1.0	i'	2020 Dec 16	53	2.0	Airmass
⋯	LCO CTIO/Sinistro	1.0	i'	2020 Dec 17	53	1.8	Airmass
⋯	LCO CTIO/Sinistro	1.0	g'	2021 Sep 21	116	1.4	Airmass, Sky/Pixel
⋯	LCO CTIO/Sinistro	1.0	i'	2021 Sep 21	116	1.8	Airmass, Sky/Pixel
TOI-2567 b	FLWO/KeplerCam	1.2	i'	2021 May 20	32	3.0	Airmass
TOI-2570 b	Grand-Pra Observatory/RCO	0.4	i'	2021 Dec 11	133	2.1	Y (T1)
⋯	LCO Teide/SBIG-6303	0.4	g'	2021 Dec 18	198	3.9	BJD_{TDB}
⋯	SUTO/OTIVAR	0.3	B	2022 Jan 10	366	4.8	Airmass, Sky/Pixel
TOI-3331 b	LCO CTIO/SBIG-6303	0.4	i'	2021 Jun 06	86	5.4	Airmass
⋯	LCO CTIO/Sinistro	1.0	g'	2021 Jun 12	104	1.5	Airmass, Sky/Pixel
⋯	LCO CTIO/Sinistro	1.0	i'	2021 Jun 12	104	1.5	Width, BJD_{TDB}
⋯	LCO CTIO/SBIG-6303	0.4	i'	2021 Jun 14	81	5.2	Airmass, FWHM
⋯	LCO CTIO/SBIG-6303	0.4	i'	2021 Jun 18	81	4.6	FWHM
⋯	Brierfield	0.36	I	2021 Jul 18	193	2.5	Airmass
⋯	Hazelwood	0.318	g'	2021 Aug 01	250	2.0	Airmass
TOI-3540 b	Acton Sky Portal	0.28	R	2021 Aug 07	26	5.3	Airmass
⋯	Villa '39	0.355	I	2021 Aug 13	179	3.0	Sky/Pixel
TOI-3693 b	OAUV/TURIA2	0.3	R	2021 Jul 19	106	6.5	None
TOI-4137 b	Grand-Pra Observatory/RCO	0.4	i'	2021 Sep 30	73	2.7	Airmass, Width

Note.
[a] Precision is computed as the rms of the residuals after subtracting the transit and detrending model.

instrument on the Southern Astrophysical Research (SOAR) 4.1 m telescope. The general observing strategy for TESS targets and data reduction procedure are described in Ziegler et al. (2019, 2021) and Tokovinin (2018), respectively, while an example SOAR observation for TOI-2193 is shown in Figure 2. Nearby stellar companions were detected in the SOAR observations for TOI-2193 (Sep. = 1.″89, $\Delta I =$ 3.8 mag); TOI-3331 (Sep. = 2.″66, $\Delta I = 2.6$ mag); and TOI-3540 (Sep. = 0.″92, $\Delta I = 1.8$ mag).

TOI-2570 was observed using the ShARCS camera on the Shane 3 m telescope at Lick Observatory (Kupke et al. 2012; Gavel et al. 2014; McGurk et al. 2014). Two sequences of observations were taken with the Shane adaptive optics system in natural guide star mode, one with a *Ks* filter ($\lambda_0 = 2.150$ μm, $\Delta\lambda = 0.320$ μm) and one with a *J* filter ($\lambda_0 = 1.238$ μm, $\Delta\lambda = 0.271$ μm). The data were reduced using the publicly available `SImMER` pipeline (Savel et al. 2020).[50] We found no evidence for stellar companions within our detection limits.

TOI-2570 and TOI-3540 were also observed in the near-infrared with the Palomar High Angular Resolution Observer (PHARO; Hayward et al. 2001) on the 200 in Hale telescope at Palomar Observatory. Both targets were observed in the Brγ filters, while TOI-3540 was also observed in the *H*cont filter. These observations improved the bound for the lack of stellar companions to TOI-2570, while also identifying the 0.″92 stellar companion to TOI-3540, as seen in the SOAR speckle images.

We observed TOI-2236 and TOI-2567 with the Zorro and 'Alopeke imaging instruments on the Gemini-South and Gemini-North telescopes, respectively (Scott & Howell 2018; Scott et al. 2021). No companions were detected in either set of observations, down to the instrumental detection limits.

Finally, the targets TOI-3693 and TOI-4137 were observed with the speckle polarimeter on the 2.5 m telescope at the Caucasian Observatory of Sternberg Astronomical Institute (SAI) of Lomonosov Moscow State University (Safonov et al. 2017). The observations were made in the *I* band, and no stellar companions were detected for either target.

2.4. High-resolution Spectroscopy

We obtained high-resolution spectroscopy for each of the 10 target systems to measure precise relative radial velocities (RVs) for each system, allowing us to confirm the planetary nature of the transiting companion and measure its mass. We sought to obtain six to eight observation epochs per target, primarily at orbital quadratures. We describe the instruments

[50] https://github.com/arjunsavel/SImMER

Table 4
TFOP SG1 Photometry

TOI	Facility	Filter	Date (UT)	BJD_{TDB}	Flux[a]	Flux Err.	Detrend Var. 1[b]	Detrend Var. 2	Detrend Var. 3
2193	Brierfield	I	2020-09-23	2459115.874574	0.987369	0.002610	−0.268009	−0.087072	⋯
2193	Brierfield	I	2020-09-23	2459115.876842	0.992802	0.002590	−0.273435	−0.093719	⋯
2193	Brierfield	I	2020-09-23	2459115.879110	0.996050	0.002600	−0.278568	−0.125733	⋯
2193	Brierfield	I	2020-09-23	2459115.881379	0.992478	0.002590	−0.283524	−0.164315	⋯
2193	Brierfield	I	2020-09-23	2459115.883647	0.993419	0.002580	−0.288294	−0.183758	⋯
2193	Brierfield	I	2020-09-23	2459115.885915	0.992296	0.002580	−0.292864	−0.213525	⋯

Notes.
[a] Flux has been normalized such that the mean out-of-transit flux has a baseline of 1.0, but is not yet detrended.
[b] The detrend variables are as listed in Table 3.

(This table is available in its entirety in machine-readable form.)

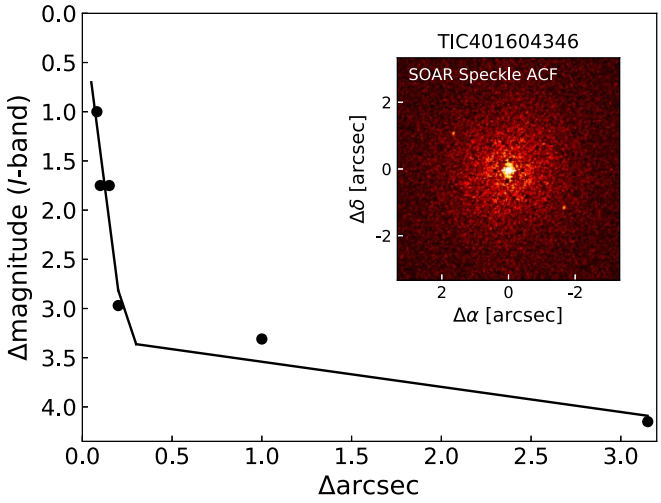

Figure 2. Speckle sensitivity curve (solid line) and autocorrelation function (ACF, inset image) from SOAR HRCam observations of TOI-2193. A nearby stellar companion is detected at 1.″89, seen as the two bright points to the northwest and southeast of the primary in the ACF image.

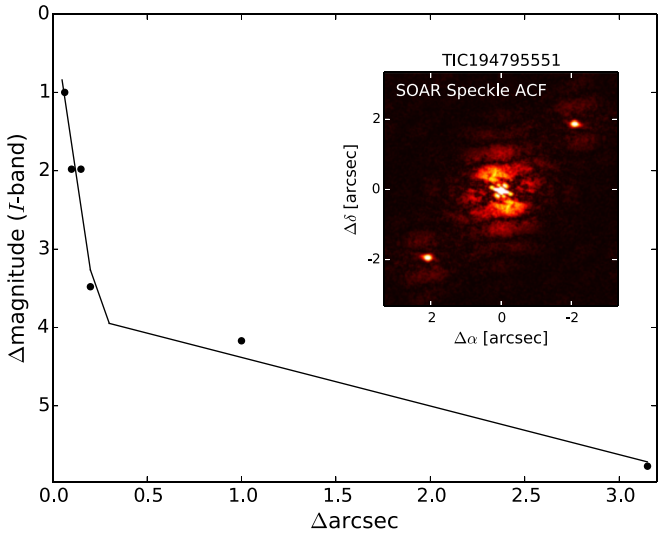

Figure 3. Same as Figure 2, but for TOI-3331. A nearby stellar companion is detected at 2.″663, visible in the inset image to the NE and SW of the primary star.

used and data analysis procedures in the rest of this section, and summarize the observations for each target in Table 6.

In addition to extracting RV measurements from each spectroscopic observation, we measured the bisector inverse slope (BIS) of the spectral line profiles, using the procedures described by Hartman et al. (2019), for the observations from the Planet Finder Spectrograph (PFS), CTIO High Resolution Spectrometer (CHIRON), Fibre-fed Optical Echelle Spectrograph (FEROS), High Resolution Echelle Spectrometer (HIRES), and NEID. For spectra that were observed through an iodine cell, we only used the iodine-free orders to perform this measurement. The complete RV and BIS data for each target are presented in Table 7, and plotted in Figures 6 and 12–20.

2.4.1. PFS Spectroscopy

We observed TOI-2193, TOI-2207, and TOI-3331 with the PFS on the 6.5 m Magellan II Clay Telescope at the Las Campanas Observatory in Chile (Crane et al. 2006, 2008, 2010). PFS is a high-resolution echelle spectrograph that uses an iodine absorption cell to produce precise radial velocities. We observed each target in the 3x3 binning mode with the iodine cell in the optical path, choosing short exposure times of 10 minutes or less, which allowed us to attain a typical RV precision of about $5\,m\,s^{-1}$, well above the instrument's demonstrated long-term precision of $\lesssim 1\,m\,s^{-1}$. The spectra were reduced and velocities extracted with the custom pipeline described by Butler et al. (1996). A high signal-to-noise ratio (S/N), iodine-free, template spectrum was also obtained for each target, as required for the RV extraction procedure.

2.4.2. CHIRON Spectroscopy

TOI-2207, TOI-2236, and TOI-2421 were observed with CHIRON (Tokovinin et al. 2013; Paredes et al. 2021) on the CTIO 1.5 m telescope on Cerro Tololo in Chile. CHIRON is an optical, fiber-fed echelle spectrometer with a spectral resolution of $R \approx 80{,}000$ when used with an image slicer. We observed with typical exposure times of 1200–1800 s, bracketed by calibration observations of a ThAr lamp. The spectra were flat-fielded, bias subtracted, and wavelength calibrated using the standard CHIRON pipeline. The radial velocities were extracted via least-squares deconvolution of the spectra against synthetic templates (Donati et al. 1997; Zhou et al. 2020), achieving a typical RV precision of 30–70 $m\,s^{-1}$. We also used the stellar parameter classification (SPC; Buchhave et al. 2012) code to derive atmospheric properties from the spectra, with the results shown in Table 9.

Table 5
Summary of High-resolution Imaging Observations

Target	Telescope	Instrument	Filter	Date	Image Type	Contrast
TOI-2193	SOAR (4.1 m)	HRCam	I_c	2020 Oct 31	Speckle	Δmag = 4.1 at 1.″0
TOI-2207	SOAR (4.1 m)	HRCam	I_c	2020 Oct 31	Speckle	Δmag = 6.3 at 1.″0
TOI-2236	Gemini-S (8 m)	Zorro	832 nm	2021 Jul 20	Speckle	Δmag = 5.3 at 0.″5
TOI-2421	SOAR (4.1 m)	HRCam	I_c	2020 Dec 03	Speckle	Δmag = 6.5 at 1.″0
TOI-2567	Gemini-N (8 m)	'Alopeke	562 nm	2021 Jun 25	Speckle	Δmag = 4.22 at 0.″5
⋯	Gemini-N (8 m)	'Alopeke	832 nm	2021 Jun 25	Speckle	Δmag = 6.18 at 0.″5
TOI-2570	Palomar (5 m)	PHARO	Brγ	2021 Nov 11	AO	Δmag = 5.325 at 0.″5
⋯	Shane (3 m)	ShARCS	J	2021 Mar 28	AO	Δmag = 3.41 at 1.″0
⋯	Shane (3 m)	ShARCS	K_s	2021 Mar 28	AO	Δmag = 4.52 at 1.″0
TOI-3331	SOAR (4.1 m)	HRCam	I_c	2021 Jul 14	Speckle	Δmag = 5.8 at 1.″0
TOI-3540	SOAR (4.1 m)	HRCam	I_c	2021 Oct 01	Speckle	Δmag = 6.7 at 1.″0
⋯	Palomar (5 m)	PHARO	Brγ	2021 Aug 24	AO	Δmag = 6.621 at 0.″5
⋯	Palomar (5 m)	PHARO	Hcont	2021 Aug 24	AO	Δmag = 7.485 at 0.″5
TOI-3693	SAI-2.5 m (2.5 m)	Speckle Polarimeter	I_c	2021 Jul 20	Speckle	Δmag = 6.1 at 1.″0
TOI-4137	SAI-2.5 m (2.5 m)	Speckle Polarimeter	I_c	2021 Oct 29	Speckle	Δmag = 5.6 at 1.″0

Table 6
Summary of Radial Velocity Measurements

Target	Instrument	N_{obs}	Median σ_{RV} (m/s)[a]	First Observation Date (UT)	Last Observation Date (UT)
TOI-2193	Magellan-Clay/PFS	8	5.8	2021 Aug 21	2021 Sep 18
TOI-2207	CTIO 1.5 m/CHIRON	16	42.5	2021 Aug 14	2021 Oct 05
⋯	MPG/FEROS	6	10.6	2021 Jul 22	2021 Oct 24
⋯	Magellan-Clay/PFS	6	5.5	2021 Aug 26	2021 Oct 19
TOI-2236	CTIO 1.5 m/CHIRON	8	70.5	2021 Aug 27	2021 Sep 29
TOI-2421	CTIO 1.5 m/CHIRON	14	29.5	2021 Aug 05	2021 Sep 29
⋯	Minerva–Australis-3	8	25.0	2021 Jul 07	2021 Aug 16
⋯	Minerva–Australis-6	3	52.0	2021 Jun 26	2021 Aug 06
TOI-2567	Keck I/HIRES	6	5.4	2021 Oct 11	2021 Nov 23
⋯	FLWO/TRES	2	41.6	2021 Apr 04	2021 Apr 19
TOI-2570	WIYN/NEID	7	6.3	2021 Nov 19	2022 Jan 07
⋯	FLWO/TRES	2	41.5	2015 Nov 30	2016 Dec 18
TOI-3331	Magellan-Clay/PFS	6	4.5	2021 Aug 26	2021 Oct 18
TOI-3540	Keck I/HIRES	6	6.0	2021 Oct 10	2021 Nov 26
⋯	FLWO/TRES	2	32.8	2021 Aug 01	2021 Aug 03
TOI-3693	Keck I/HIRES	9	6.3	2021 Oct 24	2021 Dec 26
⋯	FLWO/TRES	3	29.4	2021 Sep 05	2021 Dec 21
TOI-4137	WIYN/NEID	6	15.8	2021 Oct 30	2021 Nov 27
⋯	FLWO/TRES	2	41.3	2021 Sep 18	2021 Oct 09

Note.
[a] Median instrumental RV uncertainty for each target and instrument.

2.4.3. FEROS Spectroscopy

TOI-2207 was also observed on six epochs with the FEROS spectrograph (Kaufer et al. 1999) mounted on the MPG 2.2 m telescope at the ESO La Silla Observatory, in Chile, in the context of the Warm gIaNts with tEss collaboration (WINE; Brahm et al. 2019; Trifonov et al. 2021). FEROS is a stabilized fiber-fed high-resolution spectrograph configured with a comparison fiber to trace instrumental radial velocity drift during the scientific exposures. The six observations of TOI-2207 were performed between 2021-07-22 and 2021-10-24 with a typical exposure time of 1200 seconds, achieving an S/N per resolution element ranging from 70 to 100. All FEROS data were processed with the CERES pipeline (Brahm et al. 2017), which executed all steps involved in obtaining high-precision radial velocities with the cross-correlation technique, starting from the raw images. The typical radial velocity error of these observations was ≈10 m/s. CERES also estimates the stellar atmospheric parameters from the spectra, which are tabulated in Table 9.

2.4.4. MINERVA–Australis Spectroscopy

We also obtained 11 observations of TOI-2421 between 2021-06-26 and 2021-08-16 using the MINERVA–Australis telescope array (Wittenmyer et al. 2018; Addison et al. 2019), located at Mt. Kent Observatory, Australia. MINERVA–Australis is an array of four identical 0.7 m telescopes linked via fiber feeds to a single KiwiSpec echelle spectrograph at a spectral resolving power of $R \sim 80{,}000$ over the wavelength region of 5000–6300 Å. The array is wholly dedicated to radial velocity follow-up of TESS planet candidates (e.g., Nielsen et al. 2019; Addison et al. 2021;

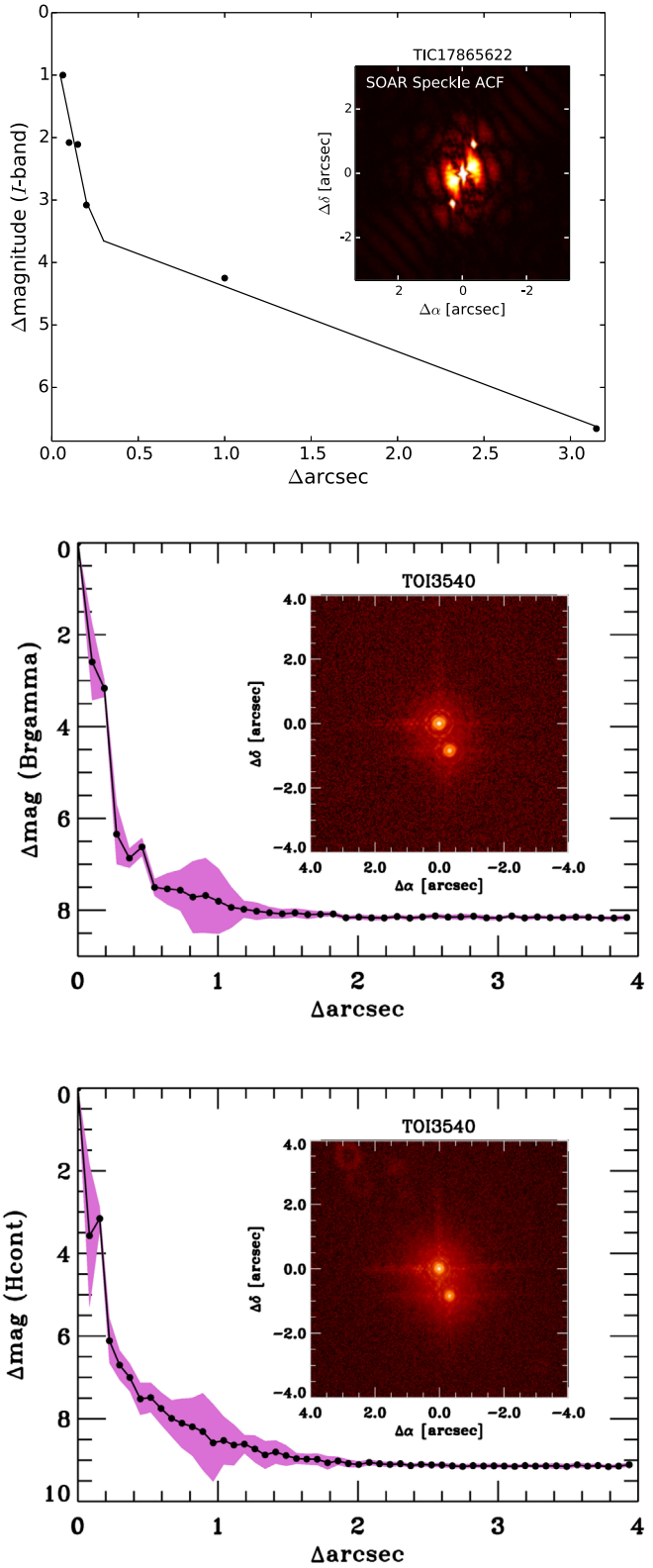

Figure 4. From top to bottom: SOAR HRCam speckle imaging, Palomar PHARO Brγ AO imaging, Palomar PHARO *H*cont AO imaging of TOI-3540. The close companion at $0\farcs92$ is detected by all three observations. The line plots in each panel show the sensitivity curves for the corresponding observation, while the shaded regions indicate the uncertainty on the contrast curve.

Wittenmyer et al. 2018). Simultaneous wavelength calibration is provided via two calibration fibers illuminated by a quartz lamp through an iodine cell. The spectra were extracted for each telescope individually, and the radial velocities were extracted via the same techniques as those described above for the CHIRON observations.

2.4.5. TRES Spectroscopy

We observed all five targets in the Northern hemisphere (TOI-2567, TOI-2570, TOI-3540, TOI-3693, and TOI-4137) with the Tillinghast Reflector Echelle Spectrograph (TRES; Fűrész 2008). TRES has a spectral resolution of $R \sim 44,000$ and is located on the FLWO 1.5 m Tillinghast Reflector telescope on Mount Hopkins, Arizona. The observations for each target were scheduled near the two opposite quadratures, ensuring maximum sensitivity to the planet's orbital motion. Two TRES spectra were taken of each target except for TOI-3693, for which we collected three observations. The data were reduced, and the radial velocities extracted using the pipeline described in Buchhave et al. (2010) and Quinn et al. (2012).

The spectra were also analyzed with SPC to derive the stellar atmospheric parameters $T_{\rm eff}$, $\log g$, [Fe/H], and $v \sin i$. The results from each observation were weighted according to the cross-correlation function and averaged together, with the final stellar properties presented in Table 9.

2.4.6. HIRES Spectroscopy

We observed TOI-2567, TOI-3540, and TOI-3693 with HIRES (Vogt et al. 1994) on the Keck I 10 m telescope on Maunakea, Hawaii. We obtained six to nine observations for each target with an iodine cell that provides a precise wavelength calibration and allows for radial velocity extraction. These observations were made through the queue system operated by the California Planet Search (CPS), and reduced with the standard CPS procedures (Howard et al. 2010; Howard & Fulton 2016).

To reduce the observation time necessary to obtain a high-S/N, iodine-free template spectrum, we used the matched template technique developed by Dalba et al. (2020). Briefly, we first obtained an iodine-free but low-S/N (~40/pixel) reconnaissance spectrum, which was then matched against a library of archival HIRES template spectra described in Yee et al. (2017). A deconvolved stellar spectral template (DSST) was then derived for the target using the high-S/N spectrum of the best-matching library star, which could then be used in the radial velocity extraction procedure. For the slowly rotating F and G dwarfs observed here, Dalba et al. (2020) found that the technique introduced a median error of 4.7 m s^{-1} to the RV measurements, compared with obtaining a high-S/N template of the target star. We included this introduced error by adding it in quadrature to the internal RV precision of the observations. For the massive planets targeted by our work, this additional error should not significantly affect the characterization of the planetary systems, especially given that we chose observation exposure times of $\lesssim$10 minutes to yield an RV precision of a similar magnitude, 5–10 m s^{-1}.

2.4.7. NEID Spectroscopy

TOI-2570 and TOI-4137 were observed with the NEID spectrograph on the WIYN 3.5 m telescope at Kitt Peak National Observatory (KPNO). NEID is a newly commissioned stabilized, fiber-fed optical spectrograph with a resolving power of $R \approx 110,000$ spanning the wavelength range from 3800 to 9300 Å. (Schwab et al. 2016; Halverson et al. 2016).

Table 7
Radial Velocity Measurements

Target	Mid-Time BJD_{TDB}	RV $m\,s^{-1}$	σ(RV) $m\,s^{-1}$	BIS $m\,s^{-1}$	σ(BIS) $m\,s^{-1}$	Instrument
TOI-2193	2459447.667662	−155.5	5.6	122	178	PFS
TOI-2193	2459449.648993	−51.0	9.2	−520	348	PFS
TOI-2193	2459452.611481	39.8	5.9	−122	222	PFS
TOI-2193	2459471.612512	−25.0	5.5	−483	294	PFS
TOI-2193	2459472.610162	17.7	5.6	−27	81	PFS

Note. The complete table of RV measurements is available in machine-readable form. The RVs presented here are relative RVs, where an independent offset for each target and instrument γ_{rel}, has been subtracted.

(This table is available in its entirety in machine-readable form.)

The data were reduced and RVs extracted using v1.1.2 of the standard NEID data reduction pipeline (NEID-DRP),[51] which derives velocities through cross correlation with a weighted numerical stellar mask based on spectral type (Baranne et al. 1996; Pepe et al. 2002). We used relatively short exposure times for our observations, obtaining RV precisions of about $5\,m\,s^{-1}$ for TOI-2570 and $15\,m\,s^{-1}$ for the relatively fainter TOI-4137.

3. Stellar Characterization

We collected literature photometry and astrometry of each of the planet host stars from the TESS input catalog (TIC; Stassun et al. 2018, 2019), Gaia Early Data Release 3 (EDR3; Brown et al. 2021; Riello et al. 2021; Lindegren et al. 2021), Two Micron All Sky Survey (2MASS; Cutri et al. 2003), Wide-field Infrared Survey Explorer (WISE; Cutri 2012), and Tycho-2 (Høg et al. 2000) catalogs. These properties are displayed in Table 8, and were used in our global modeling of each system (Section 4).

3.1. Spectroscopic Parameters

For each system, we further characterized the host star properties using the high-resolution stellar spectra obtained as part of our spectroscopic follow-up program. In the case of systems observed with the stabilized spectrographs CHIRON and NEID, we used a spectrum from a single epoch with the highest S/N. For systems observed with PFS, we used the high-S/N iodine-free template spectrum. For those observed with HIRES, we used the low-S/N iodine-free reconnaissance spectrum.

We used the publicly available code `SpecMatch-Emp` (Yee et al. 2017)[52] to obtain a homogeneous set of stellar properties for our targets. This code works by comparing a target spectrum to a library of observed high-resolution ($R \approx 60{,}000$), high-S/N ($S/N \approx 150$/pixel) spectra from Keck/HIRES. The library stars have well-determined empirical stellar properties from a variety of sources, including asteroseismology, interferometry, and spectrophotometry. The code finds the five library spectra that best match the target, accounting for rotational broadening, and interpolates between those stars' properties to derive ($T_{\rm eff}$, $R_\star$, [Fe/H]) for the target, with uncertainties of $\sigma(T_{\rm eff}) = 100$ K, $\sigma(\Delta R_\star/R_\star) = 15\%$, σ([Fe/H]) = 0.09 dex, which are robust even when the S/N is as low as 20/pixel.

While `SpecMatch-Emp` was developed for use with Keck/HIRES spectra, it has been successfully used with spectra from other instruments (e.g., Teske et al. 2018). To account for the narrow line spread functions of the other spectrographs used compared with that of HIRES, we modified the code to allow the target star's spectrum to be broadened relative to the library spectra. We found that this produced sharper χ^2 minima and a better match to the target spectrum. Previous testing of this approach using a cross-validation technique with the library Keck/HIRES spectra showed no degradation in the accuracy of the derived parameters. We compared the `SpecMatch-Emp`-derived parameters to those derived from the TRES reconnaissance spectra when available (Section 2.4.5) and found them to be within 1σ agreement.

We measured $v \sin i$ for each of the targets using the `SpecMatch-Synth`[53] (Petigura 2015) code. This code works similarly to `SpecMatch-Emp` but matches the target spectrum to a synthetic spectral library from Coelho et al. (2005) instead. A set of eight best-matching spectra are selected from the synthetic library, which spans a range of $T_{\rm eff}$, $\log g$, and [Fe/H]. These are then combined using trilinear interpolation and convolved with a rotational-macroturbulent profile and Gaussian instrumental profile to create a better match to the target spectrum. During this process, the macroturbulent broadening is assumed to follow the relationship from Valenti & Fischer (2005):

$$v_{\rm mac} = \left(3.98 - \frac{T_{\rm eff} - 5770\ {\rm K}}{650\ {\rm K}}\right) {\rm km\ s^{-1}}. \quad (1)$$

The code optimizes over the interpolation weights and $v \sin i$ to derive the target stellar atmospheric properties. We report only the $v \sin i$ from this code, but we found that the other parameters were typically within 1σ agreement with those derived by `SpecMatch-Emp`, which is more robust for low-S/N spectra. We report $T_{\rm eff}$, $\log g$, and [Fe/H] from `SpecMatch-Emp`, and $v \sin i$ and $v_{\rm mac}$ from `SpecMatch-Synth` in Table 9.

For those targets with observations from TRES, we also used SPC (Buchhave et al. 2012) to derive stellar atmospheric properties. SPC cross correlates an observed spectrum against a grid of synthetic spectra from Kurucz 1993, allowing $T_{\rm eff}$, $\log g$, [Fe/H], and $v \sin i$ to be determined. The SPC stellar parameters are also tabulated in Table 9, and we found that in all cases, the derived properties did not differ from those from `SpecMatch` by more than 1.5σ. For targets with CHIRON spectra, we derived stellar properties by matching the spectra against a library of ∼10,000 observed spectra previously classified by SPC. This procedure is described in more detail in

[51] https://neid.ipac.caltech.edu/docs/NEID-DRP
[52] https://github.com/samuelyeewl/specmatch-emp
[53] https://github.com/petigura/specmatch-syn

Table 8
Catalog Photometry and Astrometry of Planet Host Stars

Target	TOI-2193	TOI-2207	TOI-2236	TOI-2421	TOI-2567	Source
Identifiers						
TIC	401604346	90850770	394722182	70524163	258920431	
GAIA EDR3	6373308503181838592	6675883485986480256	4613145315172329984	4968289907406396160	2254929887069708160	
2MASS	20544592-7248166	20302318-4453150	01203986-8658476	02123692-3523272	19135180+6620524	
Tycho-2	9329-00167-1	7962-00808-1	9498-00283-1	7009-01148-1	⋯	
WISE	J205445.92-724816.8	J203023.20-445315.2	J012039.88-865847.8	J021236.95-352327.2	J191351.77+662052.5	
Astrometric Measurements						
R.A. (J2000)	20:54:45.895	20:30:23.207	01:20:39.841	02:12:36.966	19:13:51.759	1
Decl. (J2000)	−72:48:16.71	−44:53:15.44	−86:58:47.88	−35:23:27.31	+66:20:52.58	1
$\mu_\alpha \cos\delta$ (mas yr^{-1})	−2.465 ± 0.009	15.782 ± 0.021	−3.653 ± 0.017	29.004 ± 0.012	−16.973 ± 0.011	1
μ_δ (mas yr^{-1})	−0.911 ± 0.011	−25.806 ± 0.018	−7.860 ± 0.015	−3.689 ± 0.017	9.021 ± 0.011	1
Parallax (mas)	2.896 ± 0.009	2.626 ± 0.020	2.837 ± 0.012	3.055 ± 0.020	1.929 ± 0.009	1
b (°)	−34.782	−35.849	−30.123	−70.835	22.507	1
l (°)	320.935	355.480	302.488	243.467	97.326	1
Photometric Measurements						
T (mag)	11.400 ± 0.006	10.965 ± 0.006	10.867 ± 0.006	10.692 ± 0.006	11.749 ± 0.008	2
G (mag)	11.806 ± 0.003	11.352 ± 0.003	11.289 ± 0.003	11.157 ± 0.003	12.210 ± 0.003	1
G_{BP} (mag)	12.109 ± 0.003	11.637 ± 0.003	11.601 ± 0.003	11.510 ± 0.003	12.573 ± 0.003	1
G_{RP} (mag)	11.331 ± 0.004	10.906 ± 0.004	10.806 ± 0.004	10.637 ± 0.004	11.683 ± 0.004	1
B_T (mag)	12.857 ± 0.202	12.519 ± 0.207	12.267 ± 0.135	12.149 ± 0.089	⋯	3
V_T (mag)	12.057 ± 0.143	11.422 ± 0.102	11.664 ± 0.105	11.488 ± 0.068	⋯	3
J (mag)	10.767 ± 0.024	10.438 ± 0.024	10.261 ± 0.023	10.090 ± 0.024	11.118 ± 0.021	4
H (mag)	10.462 ± 0.023	10.201 ± 0.023	10.006 ± 0.023	9.752 ± 0.024	10.764 ± 0.019	4
K_s (mag)	10.383 ± 0.021	10.133 ± 0.023	9.960 ± 0.021	9.667 ± 0.021	10.717 ± 0.017	4
$W1$ (mag)	10.343 ± 0.023	10.091 ± 0.022	9.900 ± 0.023	9.624 ± 0.024	10.659 ± 0.023	5
$W2$ (mag)	10.354 ± 0.021	10.149 ± 0.020	9.925 ± 0.020	9.678 ± 0.020	10.714 ± 0.020	5
$W3$ (mag)	10.361 ± 0.068	10.191 ± 0.069	9.884 ± 0.037	9.623 ± 0.040	10.629 ± 0.054	5

Target	TOI-2570	TOI-3331	TOI-3540	TOI-3693	TOI-4137	Source
Identifiers						
TIC	239816546	194795551	17865622	240823272	417646390	
GAIA EDR3	3445148131761842944	4042548116644168832	1896138833241139584	404433018447476096	497750842338402560	
2MASS	05484513+3205028	18051781-3406254	21553871+2810460	01023706+5118143	05102703+7023279	
Tycho-2	⋯	7399-00615-1	⋯	3275-01223-1	4346-00736-1	
WISE	J054845.12+320502.6	J180517.84-340624.5	J215538.71+281045.9	J010237.05+511814.1	J051027.06+702327.9	
Astrometric Measurements						
R.A. (J2000)	05:48:45.129	18:05:17.800	21:55:38.729	01:02:37.054	05:10:27.093	1
Decl. (J2000)	+32:05:02.55	−34:06:25.82	+28:10:46.20	+51:18:14.00	+70:23:27.88	1
$\mu_\alpha \cos\delta$ (mas yr^{-1})	−6.531 ± 0.014	0.445 ± 0.032	6.306 ± 0.044	−6.962 ± 0.016	19.686 ± 0.013	1
μ_δ (mas yr^{-1})	−15.848 ± 0.009	−17.028 ± 0.022	−1.296 ± 0.043	−21.307 ± 0.014	−3.005 ± 0.015	1
Parallax (mas)	2.765 ± 0.014	4.446 ± 0.026	3.541 ± 0.040	5.656 ± 0.018	2.891 ± 0.017	1
b (°)	2.207	−6.219	−20.456	−11.529	17.587	1
l (°)	177.656	357.625	82.170	124.715	141.500	1
Photometric Measurements						
T (mag)	11.977 ± 0.006	11.321 ± 0.006	10.954 ± 0.007	11.419 ± 0.006	10.856 ± 0.009	2
G (mag)	12.450 ± 0.003	11.824 ± 0.003	11.428 ± 0.003	11.955 ± 0.003	11.246 ± 0.003	1
G_{BP} (mag)	12.821 ± 0.003	12.212 ± 0.003	11.674 ± 0.003	12.386 ± 0.003	11.534 ± 0.003	1
G_{RP} (mag)	11.915 ± 0.004	11.255 ± 0.004	10.835 ± 0.005	11.357 ± 0.004	10.797 ± 0.004	1
B_T (mag)	⋯	12.989 ± 0.372	⋯	12.783 ± 0.174	12.243 ± 0.093	3
V_T (mag)	⋯	11.753 ± 0.204	⋯	12.025 ± 0.120	11.395 ± 0.058	3
J (mag)	11.303 ± 0.022	10.348 ± 0.026	10.237 ± 0.021	10.657 ± 0.022	10.314 ± 0.023	4
H (mag)	10.960 ± 0.021	10.068 ± 0.029	9.899 ± 0.022	10.246 ± 0.023	10.048 ± 0.031	4
K_s (mag)	10.905 ± 0.020	9.914 ± 0.026	9.784 ± 0.017	10.151 ± 0.020	10.004 ± 0.022	4
$W1$ (mag)	10.860 ± 0.023	9.565 ± 0.022	9.742 ± 0.023	10.132 ± 0.023	9.957 ± 0.023	5
$W2$ (mag)	10.918 ± 0.020	9.653 ± 0.020	9.792 ± 0.019	10.178 ± 0.020	9.999 ± 0.021	5
$W3$ (mag)	11.178 ± 0.167	9.895 ± 0.075	9.678 ± 0.062	10.141 ± 0.049	9.930 ± 0.093	5

References (1) Gaia EDR3 (Brown et al. 2021); (2) TIC (Stassun et al. 2019); (3) Tycho-2 (Høg et al. 2000); (4) 2MASS (Cutri et al. 2003); (5) WISE (Cutri 2012). The catalog photometry presented here has not been corrected for contamination by nearby stellar companions (Section 3.2).

Table 9
Spectroscopic Stellar Properties

Target	TOI-2193	TOI-2207		TOI-2236		TOI-2421		TOI-2567		TOI-2570		TOI-3331	TOI-3540		TOI-3693		TOI-4137	
Code	SpecMatch	SpecMatch	CERES	SpecMatch	SPC	SpecMatch	SPC	SpecMatch	SPC	SpecMatch	SPC	SpecMatch	SpecMatch	SPC	SpecMatch	SPC	SpecMatch	SPC
Instrument	PFS	PFS	FEROS	CHIRON	CHIRON	CHIRON	CHIRON	HIRES	TRES	NEID	TRES	PFS	HIRES	TRES	HIRES	TRES	NEID	TRES
$T_{\rm eff}$ (K)	5974 ± 110	6075 ± 110	6050 ± 150	6228 ± 110	6164 ± 50	5645 ± 110	5577 ± 50	5609 ± 110	5650 ± 50	5756 ± 110	5765 ± 50	5521 ± 110	5865 ± 110	5969 ± 50	5246 ± 110	5274 ± 50	6125 ± 110	6134 ± 50
R_* ($R_\odot$)	1.21 ± 0.18	1.49 ± 0.22	⋯	1.66 ± 0.25	⋯	1.92 ± 0.29	⋯	1.83 ± 0.27	⋯	1.35 ± 0.20	⋯	1.06 ± 0.16	1.34 ± 0.20	⋯	0.85 ± 0.13	⋯	1.65 ± 0.25	⋯
$\log g$ (cgs)	⋯	⋯	4.20 ± 0.20	⋯	4.17 ± 0.10	⋯	3.82 ± 0.10	⋯	4.15 ± 0.10	⋯	4.43 ± 0.10	⋯	⋯	4.40 ± 0.10	⋯	4.61 ± 0.10	⋯	4.13 ± 0.10
[Fe/H] (dex)	−0.04 ± 0.09	0.15 ± 0.09	0.10 ± 0.10	0.08 ± 0.09	0.00 ± 0.10	0.18 ± 0.09	0.01 ± 0.10	0.24 ± 0.09	0.41 ± 0.08	0.18 ± 0.09	0.22 ± 0.08	0.12 ± 0.09	0.18 ± 0.09	0.30 ± 0.08	0.12 ± 0.09	−0.09 ± 0.08	0.08 ± 0.09	0.14 ± 0.08
$v \sin i$ (km s^{-1})[a]	4.6 ± 1.0	6.9 ± 1.0	7.5 ± 2.0	9.8 ± 1.0	10.2 ± 0.5	4.2 ± 1.0	5.2 ± 0.5	2.5 ± 1.0	4.6 ± 0.5	2.3 ± 1.0	4.0 ± 0.5	3.5 ± 1.0	3.9 ± 1.0	6.3 ± 0.5	4.4 ± 1.0	5.1 ± 0.5	8.8 ± 1.0	9.2 ± 0.5
$v_{\rm mac}$ (km s^{-1})[b]	3.6 ± 0.2	3.8 ± 0.2	⋯	3.2 ± 0.2	⋯	4.1 ± 0.2	⋯	4.1 ± 0.2	⋯	4.2 ± 0.2	⋯	4.1 ± 0.2	3.7 ± 0.2	⋯	4.7 ± 0.2	⋯	5.0 ± 0.2	⋯

Notes.
[a] The $v \sin i$ in the `SpecMatch` column was computed from `SpecMath-Synth`.
[b] $v_{\rm mac}$ is assumed based on effective temperature and the relation from Valenti & Fischer (2005).

Table 10
Observed Properties of Stellar Companions

	Primary	Secondary
TOI-2193		
Gaia EDR3 ID	6373308503181838592	6373308503181838080
TIC ID	401604346	1988059412
Ang. Sep. (″)	⋯	1.885
PA ({°})	⋯	124
ΔI (mag)	⋯	3.8
Parallax (mas)	2.938 ± 0.021	2.926 ± 0.087
$\mu_\alpha \cos\delta$ (mas yr^{-1})	-2.376 ± 0.029	-2.378 ± 0.120
μ_δ (mas yr^{-1})	-0.809 ± 0.037	-1.050 ± 0.165
RV (km s^{-1})	-17.8 ± 1.9	⋯
G (mag)	11.813 ± 0.000	16.047 ± 0.004
$G_{\rm BP}$ (mag)	12.127 ± 0.001	⋯
$G_{\rm RP}$ (mag)	11.340 ± 0.001	⋯
TOI-3331		
Gaia EDR3 ID	4042548116644168832	4042548120990244096
TIC ID	194795551	1565174683
Ang. Sep. (″)	⋯	2.663
PA ({°})	⋯	48
ΔI (mag)	⋯	2.6
Parallax (mas)	4.577 ± 0.057	5.388 ± 0.171
$\mu_\alpha \cos\delta$ (mas yr^{-1})	0.421 ± 0.118	10.766 ± 0.604
μ_δ (mas yr^{-1})	-16.943 ± 0.090	-22.713 ± 0.475
RV (km s^{-1})	-46.5 ± 0.6	⋯
G (mag)	11.831 ± 0.001	14.264 ± 0.002
$G_{\rm BP}$ (mag)	12.249 ± 0.003	14.999 ± 0.004
$G_{\rm RP}$ (mag)	11.268 ± 0.002	13.301 ± 0.014
TOI-3540		
Gaia EDR3 ID	1896138833241139584	⋯
TIC ID	17865622	⋯
Ang. Sep. (″)	⋯	0.917
PA ({°})	⋯	200
ΔI (mag)	⋯	1.8
ΔBrγ (mag)	⋯	1.022
ΔHcont (mag)	⋯	1.144
Parallax (mas)	3.633 ± 0.259	⋯
$\mu_\alpha \cos\delta$ (mas yr^{-1})	5.722 ± 0.496	⋯
μ_δ (mas yr^{-1})	-4.567 ± 0.592	⋯
RV (km s^{-1})	-4.1 ± 0.7	⋯
G (mag)	11.404 ± 0.003	⋯
$G_{\rm BP}$ (mag)	11.698 ± 0.002	⋯
$G_{\rm RP}$ (mag)	10.839 ± 0.003	⋯

Rodriguez et al. 2021, with results shown in Table 9. Finally, for TOI-2207, we used the CERES code (Brahm et al. 2017) to estimate stellar properties from the FEROS spectra. In all cases, the stellar properties derived by these different codes do not differ significantly, giving us greater confidence in these results. For consistency, we used the SpecMatch results for $T_{\rm eff}$, $R_\star$, and [Fe/H] for all targets as prior constraints in our EXOFASTv2 fits, as described in Section 4.

3.2. Spectral Energy Distribution Fitting for Stars with Nearby Companions

Three of the target systems (TOI-2193, TOI-3331, TOI-3540) had nearby companions detected in high-resolution imaging (Section 2.3, Figures 2–4). The magnitude difference and angular separation of the primary and secondary derived from this imaging are presented in Table 10. In the case of TOI-2193 and TOI-3331, these companions were also detected by Gaia as they are relatively bright and at separations $\gtrsim$1.″0, which Gaia can reliably resolve.

To correct the catalog photometry and photometric time-series data for contamination by these companions, we used the isochrones package (Morton 2015) to perform a multi-component spectral energy distribution (SED) fit. For each system, we fitted the blended catalog photometry, together with the Δmag between the primary and secondary stars obtained from high-resolution imaging, to synthetic photometry derived from the Modules for Experiments in Stellar Astrophysics Isochrones and Stellar Tracks (MIST) isochrones (Dotter 2016; Choi et al. 2016). We placed an error floor of 0.02 mag for the Gaia and 2MASS photometry, and 0.03 mag for the WISE photometry, to account for possible systematic errors in the isochrones in reproducing the broadband photometry measurements. The fit was additionally constrained by the parallax measurements from Gaia, the spectroscopic parameters derived for the primary in Section 3.1, and an upper limit on the line-of-sight extinction from Schlegel et al. (1998) and Schlafly & Finkbeiner (2011).

We provide the best-fit stellar properties and MIST isochrone synthetic photometry for the secondary, along with corresponding uncertainties from a Markov Chain Monte Carlo analysis, in Table 11. We then subtracted the synthetic photometry from the blended catalog photometry (as listed in Table 8), and use these corrected fluxes for our global modeling (Section 4). We also computed flux dilution factors (defined in Section 4) for each band in which time-series photometry was obtained, to correct for the contribution from the nearby stars to the light curve. These dilution factors were used in the global ExoFAST fits.

Table 11
Secondary Properties from SED Fit

	TOI-2193	TOI-3331	TOI-3540
Stellar Properties			
$T_{\rm eff}$ (K)	3913 ± 19	4172^{+260}_{-94}	4819^{+67}_{-65}
[Fe/H] (dex)	$-0.069^{+0.061}_{-0.064}$	$-0.16^{+0.13}_{-0.21}$	$0.151^{+0.073}_{-0.078}$
Age (Gyr)	7.2 ± 1.4	$7.3^{+4.2}_{-4.5}$	$6.3^{+1.6}_{-1.3}$
$M_\star$ ($M_\odot$)	0.54 ± 0.01	$0.599^{+0.025}_{-0.022}$	$0.800^{+0.020}_{-0.021}$
$R_\star$ ($R_\odot$)	$0.5126^{+0.0080}_{-0.0079}$	$0.580^{+0.022}_{-0.020}$	0.761 ± 0.013
$\log g$ (cgs)	4.7480 ± 0.0054	$4.689^{+0.017}_{-0.018}$	$4.5772^{+0.0078}_{-0.0087}$
Synthetic Photometry			
G (mag)	16.09 ± 0.02[a]	14.22 ± 0.01[a]	$13.54^{+0.10}_{-0.09}$
$G_{\rm BP}$ (mag)	16.96 ± 0.03[a]	15.01 ± 0.02[a]	14.1 ± 0.1
$G_{\rm RP}$ (mag)	15.19 ± 0.01[a]	13.36 ± 0.02[a]	$12.86^{+0.09}_{-0.08}$
T (mag)	15.15 ± 0.01[a]	13.33 ± 0.02[a]	$12.84^{+0.09}_{-0.08}$
B_T (mag)	18.38 ± 0.03	16.40 ± 0.04	15.1 ± 0.1
V_T (mag)	16.87 ± 0.03	14.90 ± 0.02	13.9 ± 0.1
J (mag)	13.98 ± 0.03	$12.20^{+0.05}_{-0.06}$	$12.02^{+0.07}_{-0.06}$
H (mag)	13.27 ± 0.03	$11.47^{+0.06}_{-0.07}$	11.46 ± 0.05
K (mag)	13.10 ± 0.03	$11.32^{+0.06}_{-0.08}$	11.38 ± 0.05
$W1$ (mag)	13.01 ± 0.03	$11.25^{+0.07}_{-0.09}$	11.34 ± 0.05
$W2$ (mag)	12.99 ± 0.03	$11.28^{+0.06}_{-0.09}$	11.40 ± 0.05
$W3$ (mag)	12.88 ± 0.03	$11.16^{+0.06}_{-0.09}$	11.32 ± 0.05

Note.
[a] We did not correct the catalog photometry for the secondary fluxes in these bands, as the primary and secondary were resolved in the Gaia catalog.

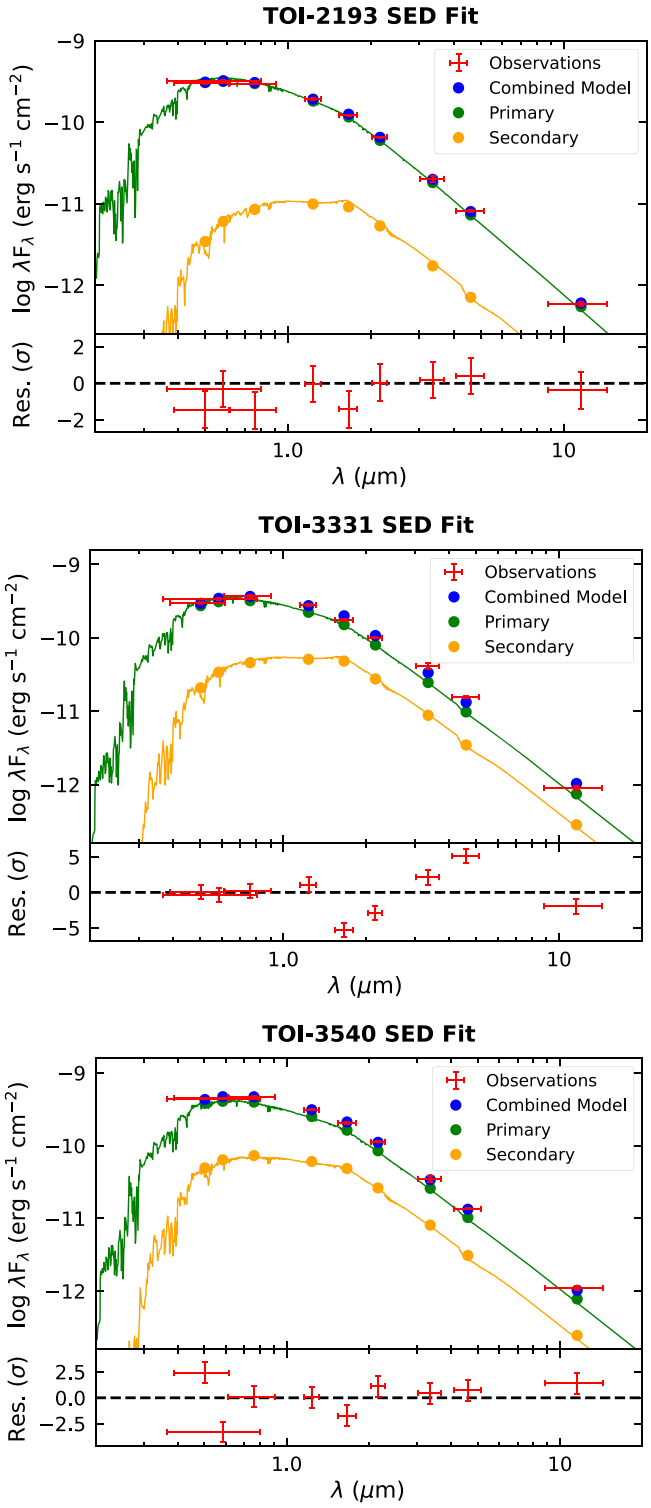

Figure 5. Multicomponent SED fits for the systems TOI-2193 (top), TOI-3331 (middle), and TOI-3540 (bottom), for which we detected nearby stellar companions. The green points show the best-fit model for the primary, while the orange points show the model for the secondary, as derived from isochrone fitting. The blue points show the combined model fluxes from both components, while the red points with error bars show the observed catalog fluxes. Extinction-corrected atmospheric models from Kurucz (1993) are plotted for the two stellar components for illustration, though these are not used directly in the fit, which is performed with the MIST bolometric correction tables. The lower panel of each plot shows the residuals of the combined observed fluxes to the combined model fit, in units of the uncertainty on each measurement.

In addition, as a further check that the spectroscopic parameters derived in Section 2.4 were not biased by possible contamination of the observed spectrum by the companion, we performed a series of tests on the `SpecMatch-Emp` code. We injected a diluted spectrum matching the companion's spectral type into the target spectrum and performed the stellar characterization procedure. We found that even if the companion was responsible for contaminating the target spectrum by up to 10%, the derived stellar properties did not vary by more than the uncertainties. Furthermore, contamination down to ∼1% would be detected in the residuals as a poor χ^2 match, which was not the case for these three targets.

We discuss each of these three targets in more detail in the rest of this section.

3.2.1. TOI-2193 Companion

The TOI-2193 system contains two stars (TOI-2193A and TOI-2193B) separated by 1.″885 and a magnitude difference of $\Delta I = 3.8$ mag. The Gaia EDR3 catalog (Brown et al. 2021; Riello et al. 2021) contains astrometry for both components, as well as three-band photometry (G, G_{BP}, G_{RP}) for the primary and G-band photometry for the secondary. The parallaxes and proper motions for the two components are identical within the uncertainties, suggesting that they are a bound system with a projected separation of ≈640 AU (Table 10). We therefore performed the `isochrone` fit assuming that the two stars have the same age and had the same initial metallicity.

The best-fit SED model found the secondary to have a mass of $M_\star = 0.54 \pm 0.01\ M_\odot$, and the estimated fluxes are shown in the top panel of Figure 5. We used this best-fit model to correct the 2MASS and WISE catalog photometry, but not the Gaia and TIC photometry, as the two components were resolved in Gaia as well as the TIC (Stassun et al. 2018, 2019). For the same reason, we do not impose an additional dilution factor for the TESS light curve, as it was already accounted for in the crowding corrections performed by the TESS SPOC.

3.2.2. TOI-3331 Companions

In the case of the TOI-3331 system, SOAR imaging detected a nearby star with an angular separation of 2.″663 and $\Delta I = 2.6$ mag. This system was also resolved by Gaia. The Gaia EDR3 catalog gives a parallax of $\Pi_2 = 5.39 \pm 0.17$ for the secondary, compared with $\Pi_1 = 4.577 \pm 0.057$ for the primary. The proper motions for the two stars differ significantly (Table 10). Thus, the two stars are most likely a chance alignment along the line of sight. Gaia photometry also resolved a third star at an angular separation of 4.″89, but we ignored this object in our fit due to its faintness ($G = 20.1$). In our isochrone fit, we model the two stars with independent ages and metallicities, with individual parallaxes as constrained by Gaia, and show the results in the middle panel of Figure 5. As with the previous case, we did not correct the Gaia and TESS photometry, as the secondary was resolved in those catalogs.

3.2.3. TOI-3540 Companion

For TOI-3540, SOAR speckle imaging as well as PHARO AO imaging both detected a companion at 0.″917, with $\Delta I = 1.8$ mag. This companion was not resolved by Gaia, so we do not have parallax or proper motion measurements for this object. However, studies (e.g., Horch et al. 2014; Matson

et al. 2018) have shown that most nearby companions within 1″ are likely to be bound, leading us to assume that this is the case for TOI-3540. This would give the pair of stars a projected separation of ≈250 au. We then performed the isochrone fit under this assumption, finding that the catalog photometry is well-described by a two-component system in which the secondary has a mass of $M_\star = 0.79 \pm 0.02\,M_\odot$. We corrected the fluxes in all photometric bands and computed the appropriate dilution factors for the TESS and ground-based time-series photometry.

4. Planetary System Characterization

We characterized each planetary system with the exoplanet fitting code EXOFASTv2 (Eastman et al. 2013, 2019). This software models the star and planet in a self-consistent manner, fitting transit and radial velocity observations as well as the broadband photometry, with constraints on the stellar properties from the MIST stellar evolutionary models (Dotter 2016; Choi et al. 2016). EXOFASTv2 uses a differential evolution Markov Chain Monte Carlo (DE-MCMC) algorithm to explore the posterior distribution and determine uncertainties of each fitted parameter.

In this section, we first describe our general fitting strategy, before describing some deviations from the general strategy for specific targets. We imposed Gaussian priors on the stellar spectroscopic properties $T_{\rm eff}$, $R_\star$, and [Fe/H] based on the SpecMatch-Emp characterization described in Section 3.1. For the SED fit, we used broadband photometry from the Gaia EDR3 (Brown et al. 2021; Riello et al. 2021), Tycho-2 (Høg et al. 2000), 2MASS (Cutri et al. 2003), and WISE (Cutri 2012) catalogs. We imposed a minimum uncertainty of 0.02 mag for the Gaia and 2MASS photometry, and 0.03 mag for the WISE photometry. We also imposed a Gaussian prior on the parallax from Gaia EDR3, corrected for the parallax zero-point as described in Lindegren et al. (2021),[54] as well as an upper limit on line-of-sight extinction from Schlegel et al. (1998) and Schlafly & Finkbeiner (2011).

We fitted the available radial velocities with an independent RV offset γ and jitter $\sigma_{\rm jit}$ terms for each instrument and target. For those targets with only two observations from TRES (TOI-2567, −2570, −3540, −4137), we did not include the TRES RVs in the fit, as the introduction of two additional free parameters per instrument did not justify their inclusion. In all cases however, we find that the TRES measurements are consistent with the modeled RV semi-amplitude from the global fit (Figures 6(c), (d), (e), and (g)), giving us additional confidence in our results. We did not allow for any long-term radial velocity trends, because our initial testing showed that trends were not required to achieve a good fit to the data for any of our systems, especially given the relatively short baseline of our RV observations.

We used both the TESS and ground-based time-series photometry to constrain the transit model. EXOFASTv2 fits an analytic transit model from Mandel & Agol (2002) and Agol et al. (2020) to the transit light curve, with quadratic limb-darkening coefficients in each band constrained by the stellar properties and the tables from Claret & Bloemen (2011) and Claret (2017). EXOFASTv2 ensures that the constraint on the stellar mean density implicit in the transit model is consistent with the mean density implied by the MIST stellar evolution model. We also fit for a separate flux baseline F_0 and added variance σ^2 for each transit light curve.

While the fluxes from TESS are already corrected for dilution from neighboring stars in the TIC (Stassun et al. 2018, 2019), we still fitted for a dilution factor A_D, to account for any inaccuracies and to propagate uncertainties, as recommended by Eastman et al. (2019). Here, $A_D = F_2/(F_1 + F_2)$ is the fractional contribution to the total flux $(F_1 + F_2)$ from all neighboring stars (F_2). We imposed a Gaussian prior on this dilution factor centered at zero and with a width equal to 10% the contamination ratio found in the TIC. For the ground-based photometry, we simultaneously detrended against the detrending vectors listed in Table 3. We normalized the detrend parameters to be between [−1, +1], and used an additive detrending model for the light curve. The final light-curve model at time i is then

$$\text{Model}_i = F_0(T_i(1 - A_D) + A_D) + \sum C_j d_{i,j}, \quad (2)$$

where T_i is the transit model with an out-of-transit baseline of 1, $d_{i,j}$ is the jth detrending parameter at time i, and C_j the additive coefficient for the jth parameter. For the TESS long-cadence data, this model is integrated over the 30 minute or 10 minute exposure time to account for smearing of the light curve over each exposure.

We performed our initial fits requiring circular orbits for each planet. We also performed a second fit in which the eccentricity was allowed to be a free parameter. In EXOFASTv2, the eccentricity is parameterized in terms of $\sqrt{e}\cos\omega$ and $\sqrt{e}\sin\omega$. In all but one case (TOI-2207b), the data are consistent with a circular orbit. As such, we adopt the results from the circular fit for these objects, but also report 1σ upper limits on the eccentricity from the fit where we allowed eccentricity to float. For TOI-2207b, our eccentric fit found that the median of the posterior distribution was more than 3σ above zero, suggesting that this planet, with an orbital period of $P \approx 8.00$ days, has a detectably eccentric orbit. We adopt the results from the eccentric fit for this target.

We ran the EXOFASTv2 DE-MCMC algorithm using the convergence criteria suggested by Eastman et al. (2019), requiring the Gelman–Rubin statistic (Gelman & Rubin 1992) to be <1.01, as well as >1000 independent draws in each parameter. Table 12 contains the median and 68% confidence intervals of the marginalized one-dimensional posterior probability distributions for the fitted stellar and planetary parameters, from the adopted fit. Additional fitted parameters specific to the observations (e.g., RV offset, jitter, and flux dilution factors) are provided in Table 13 at the end of the paper. We also provide the full results from both circular and eccentric fits for all targets as a machine-readable companion to those tables. The best-fit model for the transit, radial velocities, and SED for each system are shown in Figures 6 and and 12 through 20.

4.1. Target-specific Notes

In the case of TOI-2207 b, our eccentric fit found that the median of the posterior distribution was more than 3σ above zero, suggesting that this planet, with an orbital period of $P \approx 8.00$ days, has a detectably eccentric orbit. As such, in Table 12, we report the median and 68% confidence intervals for the eccentric fit for all parameters listed.

The objects TOI-2193A b and TOI-3540A b appear to be on orbits wherein the planetary transits graze the stellar limb. In this regime, there is a strong degeneracy between the planet-to-star radius ratio $R_p/R_\star$ and the transit impact parameter b. The

[54] https://gitlab.com/icc-ub/public/gaiadr3_zeropoint

Table 12
Median Values and 68% Confidence Intervals for Fitted Stellar and Planetary Parameters

		TOI-2193 b	TOI-2207 b	TOI-2236 b	TOI-2421 b	TOI-2567 b
Planet Parameters						
P (days)	Period	2.1225735 ± 0.0000016	$8.001968^{+0.000024}_{-0.000025}$	3.5315902 ± 0.0000026	$4.3474032^{+0.0000079}_{-0.0000078}$	5.983944 ± 0.000013
T_c ($\mathrm{BJD_{TDB}}$)	Time of conjunction	$2459052.42122 \pm 0.00021$	$2459283.82747 \pm 0.00046$	$2459011.45704 \pm 0.00023$	$2458957.02765^{+0.00064}_{-0.00063}$	$2459007.78085 \pm 0.00052$
T_{14} (days)	Transit duration	$0.06862^{+0.00087}_{-0.00084}$	$0.1930^{+0.0015}_{-0.0013}$	0.127 ± 0.001	0.2026 ± 0.0017	0.2274 ± 0.0016
τ (days)	Ingress/egress duration	$0.03431^{+0.00043}_{-0.00042}$	$0.01230^{+0.00140}_{-0.00047}$	0.0219 ± 0.0012	$0.0125^{+0.0011}_{-0.0014}$	$0.01365^{+0.00120}_{-0.00083}$
$a/R_\star$	Planet-star separation	$5.71^{+0.17}_{-0.13}$	11.7 ± 0.4	$6.84^{+0.16}_{-0.15}$	$6.67^{+0.34}_{-0.24}$	$8.64^{+0.24}_{-0.31}$
$(R_P/R_\star)^2$	Transit depth	$0.0191(>0.0169)$	$0.004273^{+0.000098}_{-0.000090}$	$0.007011^{+0.000092}_{-0.000090}$	$0.002949^{+0.000071}_{-0.000075}$	$0.003537^{+0.000073}_{-0.000068}$
i (deg)	Inclination	$79.96(<80.57)$	$88.84^{+0.79}_{-0.85}$	$83.58^{+0.26}_{-0.25}$	$86.49^{+1.30}_{-0.76}$	$88.30^{+1.10}_{-0.82}$
K (m/s)	RV semi-amplitude	136^{+25}_{-26}	$55.8^{+8.3}_{-10.0}$	172 ± 43	$37.8^{+8.6}_{-8.9}$	$20.6^{+3.2}_{-3.1}$
a (AU)	Semimajor axis	$0.03319^{+0.00052}_{-0.00051}$	$0.0854^{+0.0015}_{-0.0016}$	$0.05009^{+0.00080}_{-0.00082}$	$0.0543^{+0.0021}_{-0.0010}$	$0.0672^{+0.0024}_{-0.0012}$
R_P (R_J)	Planet radius	$1.77(>1.55)$	$0.995^{+0.028}_{-0.027}$	$1.282^{+0.032}_{-0.031}$	$0.925^{+0.035}_{-0.034}$	$0.975^{+0.031}_{-0.029}$
M_P (M_J)	Planet mass	0.94 ± 0.18	$0.64^{+0.10}_{-0.12}$	$1.58^{+0.40}_{-0.39}$	0.333 ± 0.079	$0.201^{+0.034}_{-0.031}$
ρ_P (g cm^{-3})	Planet density	$0.060(<0.321)$	0.80 ± 0.16	$0.93^{+0.25}_{-0.24}$	$0.52^{+0.15}_{-0.13}$	$0.269^{+0.052}_{-0.051}$
$\log g_P$ (cgs)	Planet surface gravity	$2.81(<3.00)$	$3.203^{+0.071}_{-0.092}$	$3.38^{+0.10}_{-0.12}$	$2.98^{+0.10}_{-0.12}$	$2.720^{+0.071}_{-0.080}$
$b \equiv a\cos i/R_\star$	Transit impact parameter	$0.990(>0.967)$	$0.20^{+0.16}_{-0.14}$	$0.766^{+0.013}_{-0.014}$	$0.409^{+0.071}_{-0.130}$	$0.26^{+0.11}_{-0.16}$
e	Eccentricity	0.0 (fixed)	$0.174^{+0.048}_{-0.052}$	0.0 (fixed)	0.0 (fixed)	0.0 (fixed)
e_{lim}[a]	1σ upper limit on eccentricity	<0.063	...	<0.135	<0.136	<0.080
τ_{circ} (Gyr)[b]	Tidal circularization timescale	$0.00036(<0.00908)$	$13.2^{+5.6}_{-4.6}$	$0.40^{+0.12}_{-0.11}$	$0.94^{+0.37}_{-0.28}$	$1.78^{+0.44}_{-0.43}$
$\langle F\rangle$ (Gerg s^{-1} cm^{-2})	Incident flux	2.20 ± 0.11	$0.553^{+0.026}_{-0.024}$	$1.846^{+0.085}_{-0.088}$	$1.257^{+0.065}_{-0.088}$	$0.759^{+0.042}_{-0.041}$
T_{eq} (K)	Planet equilibirum temperature	1763^{+21}_{-22}	1259^{+16}_{-15}	1688^{+19}_{-21}	1534^{+20}_{-28}	1352^{+18}_{-19}
Stellar Parameters						
$M_\star$ ($M_\odot$)	Stellar mass	$1.082^{+0.052}_{-0.049}$	$1.296^{+0.069}_{-0.072}$	$1.343^{+0.066}_{-0.065}$	$1.131^{+0.130}_{-0.064}$	$1.130^{+0.130}_{-0.059}$
$R_\star$ ($R_\odot$)	Stellar radius	$1.248^{+0.026}_{-0.028}$	$1.564^{+0.041}_{-0.040}$	1.573 ± 0.033	$1.750^{+0.051}_{-0.049}$	$1.686^{+0.043}_{-0.044}$
$\log g_\star$ (cgs)	Stellar surface gravity	$4.278^{+0.030}_{-0.024}$	$4.161^{+0.034}_{-0.036}$	4.172 ± 0.024	$4.005^{+0.059}_{-0.037}$	$4.044^{+0.036}_{-0.037}$
$\rho_\star$ (g cm^{-3})	Stellar density	$0.781^{+0.072}_{-0.052}$	$0.476^{+0.050}_{-0.047}$	$0.486^{+0.034}_{-0.031}$	$0.297^{+0.048}_{-0.031}$	$0.340^{+0.030}_{-0.036}$
$L_\star$ ($L_\odot$)	Stellar luminosity	$1.779^{+0.075}_{-0.084}$	3.05 ± 0.11	$3.41^{+0.14}_{-0.18}$	$2.729^{+0.095}_{-0.091}$	2.54 ± 0.11
T_{eff} (K)	Stellar effective temperature	5966^{+73}_{-72}	6101^{+75}_{-73}	6248^{+72}_{-77}	5607 ± 68	5611^{+62}_{-65}
[Fe/H] (dex)	Metallicity	$0.027^{+0.066}_{-0.052}$	0.181 ± 0.086	$0.119^{+0.081}_{-0.078}$	$0.190^{+0.083}_{-0.085}$	$0.241^{+0.078}_{-0.079}$
$[\mathrm{Fe/H}]_0$ (dex)[c]	Initial metallicity	$0.082^{+0.060}_{-0.052}$	0.245 ± 0.081	0.222 ± 0.072	$0.210^{+0.076}_{-0.083}$	$0.258^{+0.071}_{-0.073}$
Age (Gyr)	Stellar age	$5.5^{+1.9}_{-1.7}$	$3.3^{+1.3}_{-1.1}$	$2.52^{+0.89}_{-0.82}$	$7.5^{+1.7}_{-2.8}$	$7.6^{+1.8}_{-2.7}$
EEP[d]	Equal evolutionary phase	404^{+16}_{-28}	383^{+30}_{-33}	360^{+30}_{-15}	$455.6^{+4.5}_{-37.0}$	$452.6^{+5.2}_{-33.0}$
A_V (mag)	Visual extinction	$0.113^{+0.045}_{-0.060}$	$0.049^{+0.031}_{-0.032}$	$0.305^{+0.040}_{-0.064}$	$0.024^{+0.013}_{-0.015}$	$0.074^{+0.030}_{-0.042}$
d (pc)	Distance	345.3 ± 1.1	380.6 ± 2.9	352.4 ± 1.5	$328.1^{+4.2}_{-4.0}$	$505.2^{+7.7}_{-7.4}$

Table 12
(Continued)

		TOI-2570 b	TOI-3331 b	TOI-3540 b	TOI-3693 b	TOI-4137 b
Planet Parameters						
P(days)	Period	2.9887615 ± 0.0000022	$2.0180231^{+0.0000043}_{-0.0000044}$	3.1199990 ± 0.0000079	$9.088516^{+0.000026}_{-0.000027}$	3.8016122 ± 0.0000065
T_c (BJD_{TDB})	Time of conjunction	$2459393.14532 \pm 0.00021$	2459371.6530 ± 0.0002	$2459109.14114 \pm 0.00089$	$2458806.68164^{+0.00032}_{-0.00031}$	$2458990.46651 \pm 0.00033$
T_{14} (days)	Transit duration	$0.12527^{+0.00097}_{-0.00091}$	$0.08846^{+0.00085}_{-0.00083}$	$0.0792^{+0.0026}_{-0.0025}$	$0.1482^{+0.0012}_{-0.0011}$	0.1429 ± 0.0013
τ (days)	Ingress/egress duration	$0.01423^{+0.00093}_{-0.00089}$	$0.01397^{+0.00087}_{-0.00084}$	0.0396 ± 0.0013	$0.01937^{+0.00100}_{-0.00052}$	$0.0167^{+0.0012}_{-0.0011}$
$a/R_\star$	Planet-star separation	$8.13^{+0.23}_{-0.22}$	$7.09^{+0.18}_{-0.17}$	$7.51^{+0.26}_{-0.25}$	$22.13^{+0.30}_{-0.47}$	7.80 ± 0.24
$(R_P/R_\star)^2$	Transit depth	0.01304 ± 0.00026	0.01559 ± 0.00033	$0.023(>0.015)$	$0.02134^{+0.00041}_{-0.00039}$	0.00749 ± 0.00014
i (deg)	Inclination	$87.73^{+0.75}_{-0.57}$	$85.40^{+0.38}_{-0.36}$	$81.93(<83.11)$	$89.57^{+0.29}_{-0.28}$	85.7 ± 0.4
K (m/s)	RV semi-amplitude	$111.2^{+6.9}_{-7.5}$	360 ± 21	155^{+17}_{-16}	109^{+26}_{-24}	156^{+17}_{-15}
a (AU)	Semimajor axis	$0.04145^{+0.00081}_{-0.00086}$	$0.03144^{+0.00048}_{-0.00055}$	$0.04289^{+0.00092}_{-0.00093}$	$0.0813^{+0.0011}_{-0.0012}$	$0.05222^{+0.00089}_{-0.00096}$
R_P (R_J)	Planet radius	$1.217^{+0.035}_{-0.034}$	1.158 ± 0.043	$2.10(>1.44)$	$1.124^{+0.029}_{-0.023}$	$1.211^{+0.040}_{-0.039}$
M_P (M_J)	Planet mass	$0.820^{+0.063}_{-0.065}$	2.27 ± 0.16	1.18 ± 0.14	$1.02^{+0.24}_{-0.22}$	$1.44^{+0.17}_{-0.15}$
ρ_P (g cm^{-3})	Planet density	$0.563^{+0.069}_{-0.063}$	$1.82^{+0.24}_{-0.21}$	$0.065(<0.512)$	$0.89^{+0.22}_{-0.20}$	$1.01^{+0.17}_{-0.15}$
$\log g_P$ (cgs)	Planet surface gravity	$3.137^{+0.041}_{-0.043}$	3.624 ± 0.041	$2.64(<3.17)$	$3.300^{+0.095}_{-0.110}$	$3.387^{+0.057}_{-0.058}$
$b \equiv a \cos i/R_\star$	Transit impact parameter	$0.32^{+0.07}_{-0.10}$	$0.569^{+0.030}_{-0.034}$	$1.073(>0.936)$	$0.17^{+0.10}_{-0.11}$	$0.584^{+0.035}_{-0.038}$
e	Eccentricity	0.0 (fixed)	0.0 (fixed)	0.0 (fixed)	0.0 (fixed)	0.0 (fixed)
$e_{\rm lim}$[a]	1σ upper limit on eccentricity	< 0.039	< 0.188	< 0.164	< 0.054	< 0.246
$\tau_{\rm circ}$ (Gyr)[b]	Tidal circularization timescale	$0.111^{+0.022}_{-0.018}$	$0.071^{+0.015}_{-0.012}$	$0.0027(<0.0897)$	$22.3^{+6.0}_{-5.4}$	$0.66^{+0.16}_{-0.13}$
$\langle F \rangle$ (Gerg s^{-1} cm^{-2})	Incident flux	$0.951^{+0.066}_{-0.060}$	$1.114^{+0.096}_{-0.083}$	$1.145^{+0.069}_{-0.066}$	$0.0934^{+0.0064}_{-0.0056}$	$1.379^{+0.092}_{-0.082}$
$T_{\rm eq}$ (K)	Planet equilibirum temperature	1431^{+24}_{-23}	1488^{+31}_{-29}	1498 ± 22	801^{+13}_{-12}	1570^{+25}_{-24}
Stellar Parameters						
$M_\star$ ($M_\odot$)	Stellar mass	$1.063^{+0.063}_{-0.065}$	$1.016^{+0.047}_{-0.052}$	$1.081^{+0.071}_{-0.069}$	$0.867^{+0.036}_{-0.037}$	$1.313^{+0.068}_{-0.071}$
$R_\star$ ($R_\odot$)	Stellar radius	$1.095^{+0.026}_{-0.025}$	0.952 ± 0.029	1.228 ± 0.033	$0.791^{+0.017}_{-0.014}$	$1.438^{+0.039}_{-0.038}$
$\log g_\star$ (cgs)	Stellar surface gravity	$4.385^{+0.030}_{-0.031}$	$4.487^{+0.022}_{-0.023}$	4.293 ± 0.036	$4.581^{+0.014}_{-0.021}$	$4.240^{+0.031}_{-0.032}$
$\rho_\star$ (g cm^{-3})	Stellar density	$1.138^{+0.100}_{-0.091}$	$1.65^{+0.13}_{-0.12}$	$0.823^{+0.090}_{-0.079}$	$2.48^{+0.10}_{-0.16}$	$0.621^{+0.059}_{-0.055}$
$L_\star$ ($L_\odot$)	Stellar luminosity	$1.199^{+0.086}_{-0.079}$	$0.807^{+0.081}_{-0.068}$	$1.549^{+0.079}_{-0.080}$	$0.453^{+0.034}_{-0.030}$	$2.75^{+0.20}_{-0.17}$
$T_{\rm eff}$ (K)	Stellar effective temperature	5771^{+89}_{-87}	5609^{+92}_{-87}	5810 ± 79	5321^{+86}_{-82}	6202^{+94}_{-90}
[Fe/H] (dex)	Metallicity	0.191 ± 0.083	0.148 ± 0.084	0.176 ± 0.089	$0.071^{+0.079}_{-0.076}$	$0.182^{+0.083}_{-0.085}$
$[Fe/H]_0$ (dex)[c]	Initial metallicity	0.193 ± 0.075	0.13 ± 0.08	$0.204^{+0.077}_{-0.078}$	$0.050^{+0.078}_{-0.075}$	0.247 ± 0.068
Age(Gyr)	Stellar age	$4.4^{+3.3}_{-2.6}$	$2.1^{+2.7}_{-1.5}$	$6.0^{+3.0}_{-2.5}$	$3.0^{+3.8}_{-2.1}$	$2.1^{+1.3}_{-1.0}$
EEP[d]	Equal evolutionary phase	366^{+35}_{-32}	328^{+21}_{-38}	406^{+20}_{-37}	323^{+22}_{-36}	347^{+37}_{-18}
A_V (mag)	Visual extinction	$0.255^{+0.089}_{-0.092}$	$0.21^{+0.14}_{-0.13}$	$0.130^{+0.043}_{-0.065}$	0.2 ± 0.1	$0.132^{+0.081}_{-0.072}$
d (pc)	Distance	361.7 ± 1.8	224.6 ± 1.3	$282.6^{+3.2}_{-3.1}$	$176.5^{+1.5}_{-1.4}$	$333.6^{+4.2}_{-4.1}$

Notes. This table contains the fit results from the preferred fit for each target: circular fits (e fixed at 0.0) for all targets apart from TOI-2207b, and an eccentric fit for TOI-2207b. For TOI-2193A b and TOI-3540A b, we provide the posterior mode and 95% lower limits for the $(R_p/R_\star)^2$, R_p, and b, and the posterior mode and 95% upper limits for i, ρ_P,$\log g_P$, and $\tau_{\rm circ}$. Table 3 in Eastman et al. (2019) provides a detailed description of all derived and fitted parameters.

[a] For those targets where we adopt a circular fit, we also provide the 68% upper limit on eccentricity derived from the eccentric fits.

[b] The tidal circularization timescale is computed with Equation (3) of Adams & Laughlin (2006), assuming a tidal quality factor $Q_S = 10^6$.

[c] The stellar metallicity when the star was formed, which is defined by the grid points for the MIST stellar evolutionary tracks.

[d] The equal evolutionary phase (EEP) corresponds to specific points in the stellar evolutionary tracks, as described in Dotter (2016). Table 12 is published in its entirety in the electronic edition of the *Astrophysical Journal*. This version only shows the results from the preferred fit for each target. The full version includes these results and fits where the eccentricity was allowed to float. Note that the full version also includes the results from the additional fit parameters outlined in Table 13.

(This table is available in its entirety in machine-readable form.)

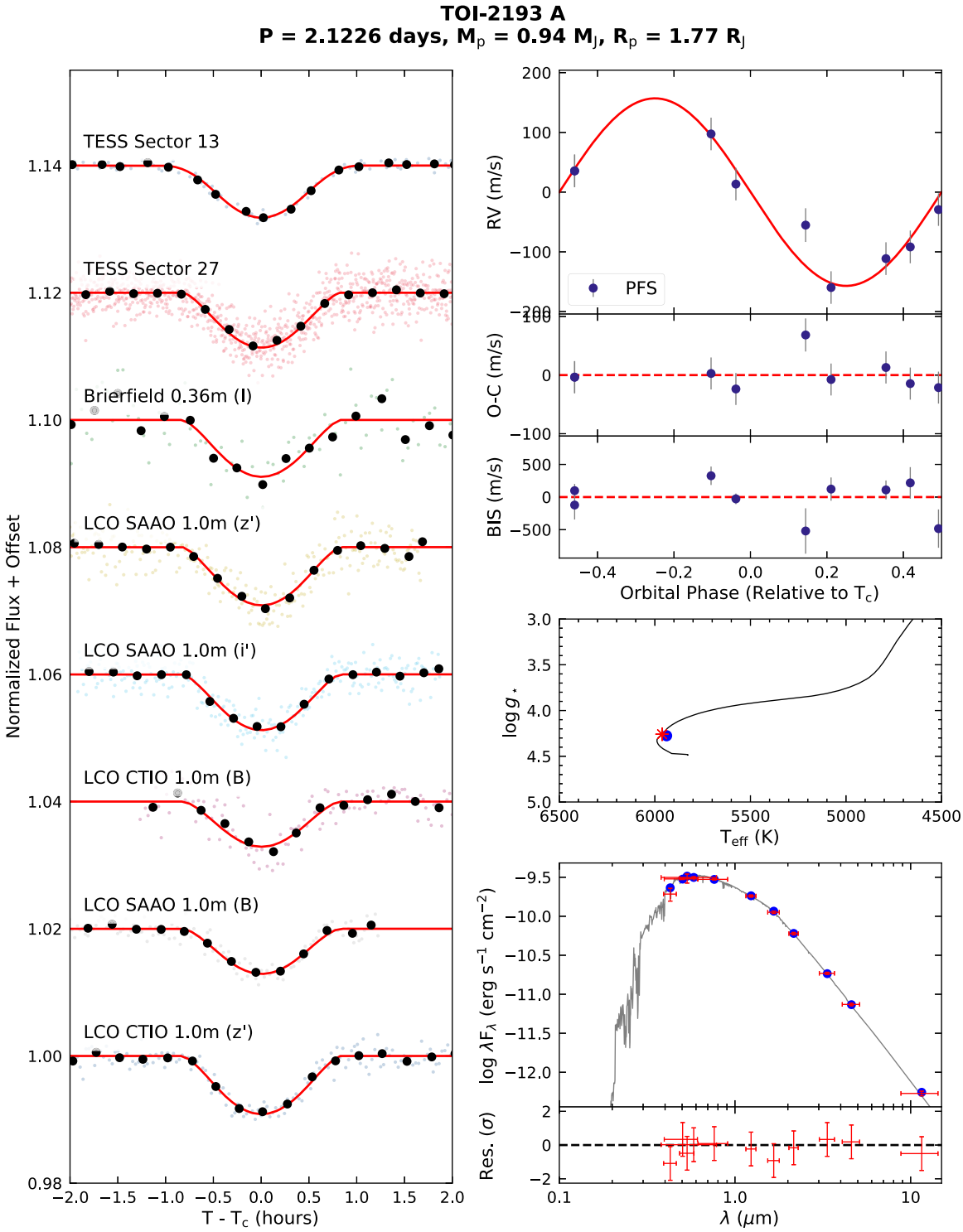

Figure 6. Results of EXOFASTv2 fits for TOI-2193. Left: TESS and ground-based photometric observations, phased to the best-fit orbital period and time of conjunction. The black points are the photometric time-series data binned to 15 min cadence, while the faint colored points are the unbinned data. The red line shows the best-fit transit model, corrected for flux dilution and additive detrending. Top right: Radial velocity observations of TOI-2193, phased to the best-fit orbital period. The error bars reflect the internal measurement error added in quadrature to the fitted jitter $\sigma_{\rm jit}$ parameter for each instrument. The two lower subpanels show the phased radial velocity residuals and bisector span measurements. Middle right: The best-fit MIST stellar evolution track (black line), which is fit simultaneously and self-consistently with the transit and RV model. The blue point shows the best-fit stellar $T_{\rm eff}$ and $\log g$, while the red asterisk corresponds to the star's position along the track given its best-fit age. The small discrepancies between the two are well within the fitted uncertainties in each parameter. Lower right: Result of the SED fit, performed using the MIST bolometric correction grid. The red points are the catalog broadband photometric measurements, corrected for the presence of any stellar companions (i.e., subtracting the yellow points in Figure 5), with vertical error bars showing the catalog uncertainty and horizontal error bars showing the bandpass width. The model fluxes in each bandpass, derived from the MIST grid, are the blue points. An atmospheric model from Kurucz (1993) corresponding to the best-fit stellar parameters is plotted in gray for illustrative purposes only and is not used directly in the fit. The lower subpanel shows the residuals to the model fit, in units of the uncertainty on each measurement.

resulting posterior distributions for these parameters have long tails allowing for extremely large and unphysical planet radii. In these cases, we placed an upper limit of $R_p/R_\star < 0.5$ during the fit to ensure convergence of the MCMC fits within these limits. As the medians of the posterior distributions would be heavily skewed by the long tails, we report the mode of the posterior distributions and the 95% lower limit on the planet radius and 95% upper limit on the orbital inclination (note that these limits also depend on the cutoff chosen during the fit).

In general, we did not fit for any dilution factors in the transit light curves, except for the TESS data, where we allowed A_D to vary within a small range around zero. However, for the targets described in Section 3.2 that have stellar companions, we also allowed for dilution of the ground-based light curves, as the apertures used also contained the stellar companions. In these cases, we used the best-fit multicomponent SED model to derive dilution factors for each photometric filter to correct the light curves, imposing a Gaussian prior with width equal to 10% of the dilution factor around the mean value.

For targets observed in multiple TESS sectors, we generally fit each sector of data separately, with a separate baseline flux F_0 and variance σ^2 per sector. TOI-2567 was observed by TESS in a total of 15 sectors (14–26, 40, 41), which would greatly increase the dimensionality of the fit were we to include these two additional free parameters for each. In this case, we fit the Sectors 14–26 data, which were all at 30 min cadence, as a single light curve. The sectors 40 and 41 data were taken at 2 min cadence, and we fit these as a single light curve too. In general, our fitted values for F_0 and σ^2 for the TESS data are close to 1.0 and 0.0, respectively, indicating minimal baseline offsets between sectors, so combining these consecutive sectors of data should not have had a significant impact on the fit.

4.2. Potential False-positive Scenarios

Various astrophysical phenomena can lead to light curves that appear similar to planetary transits, leading to false-positive planet detections (e.g., Collins et al. 2018). The goal of our ground-based follow-up observations was to help rule out or reduce the likelihood of such scenarios. For each of our 10 hot Jupiter systems, the seeing-limited ground-based photometry confirm that the transits occur on the target stars, as opposed to being nearby eclipsing binaries that contaminate the TESS photometric aperture. The measured RV semi-amplitudes for all companions are also consistent with planetary mass objects, rather than brown dwarfs, which can have similar radii despite their significantly larger masses. Furthermore, the spectra of each target showed no indications of secondary spectral lines. To check for the possibility of unresolved blended eclipsing binaries causing line-profile variations that may appear as RV variations, we computed the Pearson-r coefficient to check for correlations between the measured RV and the spectral line BIS. For each of the 10 target systems, we found no statistically significant correlations ($p > 0.1$).

Given the extensive ground-based follow-up observations and lack of BIS variations, we are confident that all of our targets are confirmed as true planets. However, we chose to pay closer attention to the two systems TOI-2193 and TOI-3540, which exhibit grazing transits and have close resolved stellar companions. Although the measured RV reflex motions measured on the primary stars are indicative of planetary mass objects orbiting them, there may be concern that these may actually be blended

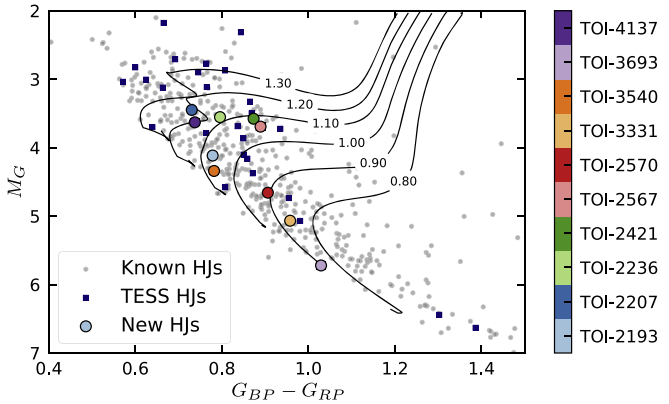

Figure 7. Gaia absolute G-magnitude and $G_{BP} - G_{RP}$ color–magnitude diagram for known hot Jupiter hosts in the NASA Exoplanet Archive. The colored circles are the 10 systems presented in this paper, identified by the color bar on the right (these colors are consistent with the following figures). The navy blue squares show hot Jupiter systems discovered by TESS, while the gray circles show the remaining hot Jupiter systems. The black lines show the MIST evolutionary tracks at a metallicity of [Fe/H] = + 0.15, close to the median metallicity of our sample, for stellar masses between 0.8 and 1.30 $M_\odot$. The points have not been corrected for interstellar extinction.

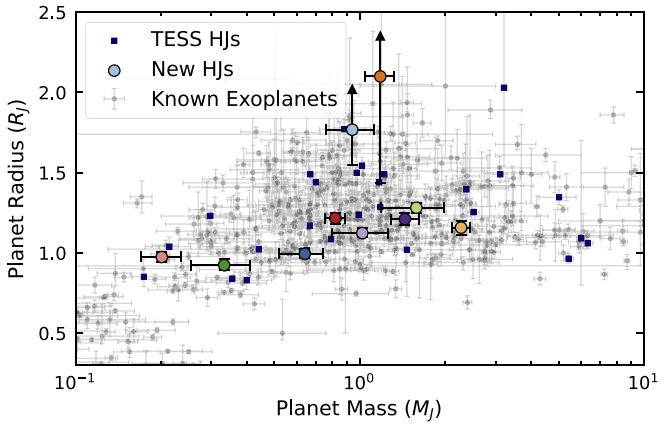

Figure 8. Mass–radius distribution for the systems presented in this paper (colored circles). For TOI-2193A b and TOI-3540b, we plot the mode and lower limits on the planet radii. The navy blue squares show hot Jupiter systems discovered by TESS, while the gray circles show the masses and radii of all planets from the NASA Exoplanet Archive (not just hot Jupiters) with masses determined to better than 50% and radii to better than 20%.

eclipsing binary (EB) false positives, where the diluted light of the companion is the source of both the transit and apparent radial velocity variations. In the case of TOI-2193, the nearby companion TOI-2193B is 1.″885 away. A small aperture measurement (1.″2) of the LCO–CTIO light curve taken on UT 2021-07-26 confirmed that the source of the transit signal is indeed TOI-2193A. For TOI-3540, the companion star is just 0.″917 away and could not be resolved by seeing-limited photometry.

In order to definitively rule out such scenarios for these two objects, we carried out a detailed blend modeling of each system following the procedures described in Hartman et al. (2019), which is based on the work of Torres et al. (2004). In each case we jointly model the available TESS and ground-based light curves, catalog broadband photometry, Gaia parallaxes, and spectroscopically determined atmospheric parameters. We include the resolved stellar companions in the modeling, jointly fitting for the masses, metallicities, distances, and ages of all stars that we assume

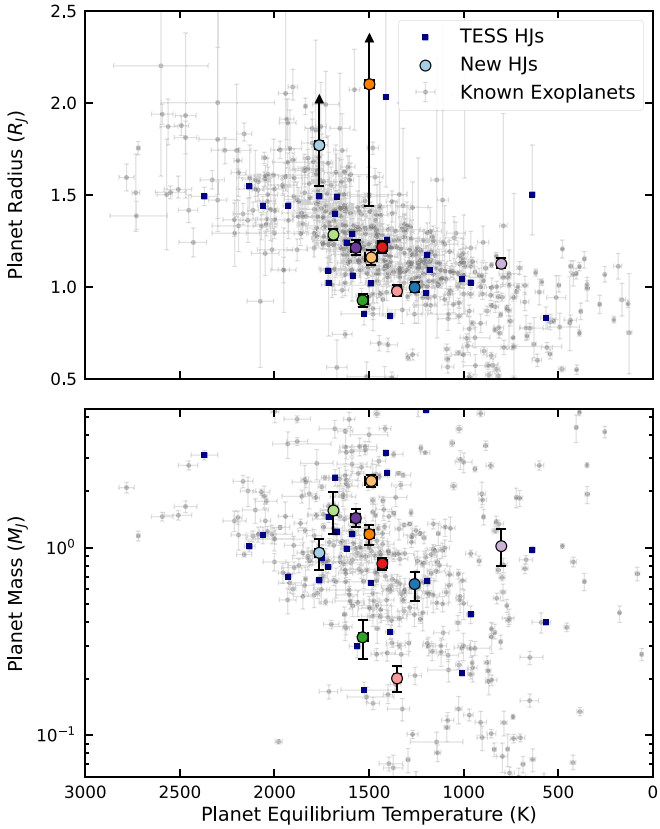

Figure 9. Distribution of planet radius (top panel) and mass (lower panel) as a function of planet insolation, expressed as the equilibrium temperature at the planet's orbital distance, assuming no albedo and perfect heat redistribution. The two least massive planets in our sample, TOI-2421b and TOI-2567b, lie on the lower edge of the distribution of known hot Jupiters, just above the hot Neptune desert (Mazeh et al. 2016). The navy blue squares and gray circles represent the same previously known systems as described in Figure 8.

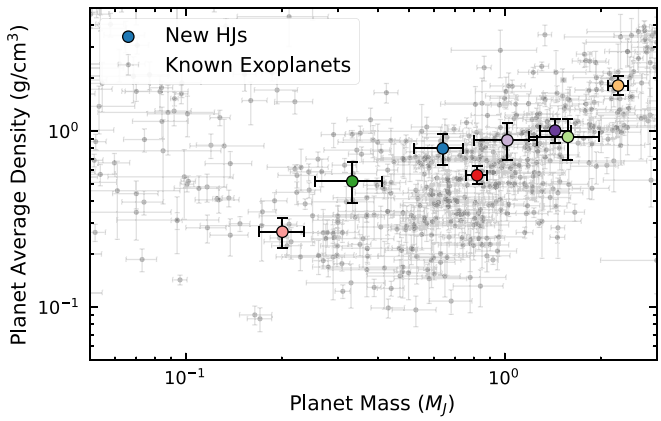

Figure 10. Bulk density of the planets in our sample, excluding the grazing planets TOI-2193A b and TOI-3540b. The gray circles represent the same previously known systems as described in Figure 8.

contribute to the blended (or resolved) measurements, and we include the measured magnitude differences from high-resolution imaging as observations to be fit in the modeling. We use the MIST stellar models to constrain the properties of the stars. For TOI-2193 we force the resolved stellar companion to have the same age, distance, and metallicity as the primary star, while for TOI-3540 we allow the components to have independent values.

For each system we consider four scenarios: (1) the primary object in the resolved pair is a single star with a transiting planet, while the secondary object is also a single star; (2) the primary object in the resolved pair is a single star, while the secondary object is a two-component stellar eclipsing binary system; (3) the primary object in the resolved pair is itself an unresolved hierarchical triple consisting of a bright noneclipsing star and a fainter stellar eclipsing binary, and the secondary object in the resolved pair is a single star; and (4) the primary object in the resolved pair is an unresolved blend between a bright noneclipsing star and a line-of-sight background eclipsing binary, while the secondary object in the resolved pair is a single star. For both TOI-2193 and TOI-3540 we find that scenario (1) provides the best (lowest χ^2) fit to the observations, despite using the fewest model parameters. In both cases the combination of the photometry and Gaia parallax measurements favors scenarios where each of the resolved point sources is itself a single star, while the transit duration and depth, and the lack of secondary eclipses or ellipsoidal variations in the light curves favors a transiting planet around the primary star over scenarios involving eclipsing stellar binaries. For both TOI-2193 and TOI-3540 we find that scenario (4) is the next-best-fitting scenario, and that this scenario has $\Delta\chi^2 \approx 70$, and $\Delta\chi^2 \approx 9$ compared to scenario (1) for TOI-2193 and TOI-3540, respectively. The relative inability of the blend-models to fit the photometric data, together with the significant RV variations consistent with transiting giant planet companions, and the lack of any significant BIS variation in phase with the transit ephemerides, leads us to conclude that both TOI-2193A b and TOI-3540A b have been confirmed as transiting planets.

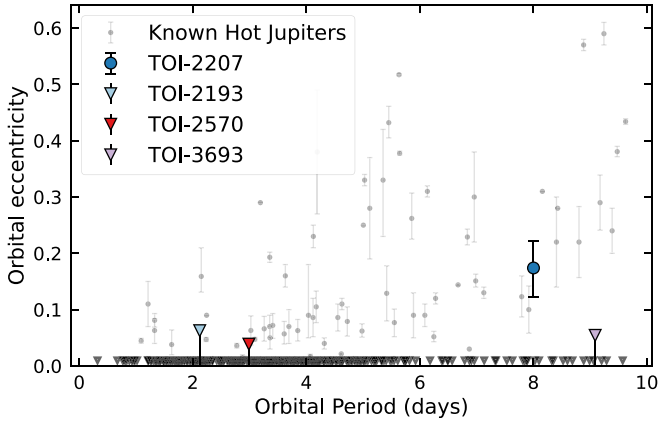

Figure 11. Measured eccentricities and upper limits for the planets in our sample. Here, we show the 68% confidence interval measured for the eccentricity of TOI-2207b, along with 68% upper limits on the eccentricity for TOI-2193b, TOI-2570b, and TOI-3693b, for which we can place a constraint better than $e < 0.1$ from the current data. The gray circles show the measured eccentricities of previously known giant exoplanets ($R_p > 8R_\oplus$) with eccentricities at least 2σ greater than zero, while gray triangles at the bottom of the plot show planets on orbits consistent with circular orbits.

5. Discussion

The 10 planets presented in this paper have orbital periods between 2 and 10 days, and masses between 0.2 and 2.2 M_J. To put these newly discovered planets into context, we downloaded data from the NASA Exoplanet Archive (NASA Exoplanet Archive 2022).[55]

In Figure 7, we show the distribution of the stellar hosts of our 10 planets in color–magnitude space, in the context of other hot Jupiter hosts (orbital period $P < 10$ days, planet radius

[55] https://exoplanetarchive.ipac.caltech.edu/, accessed 14 February 2022.

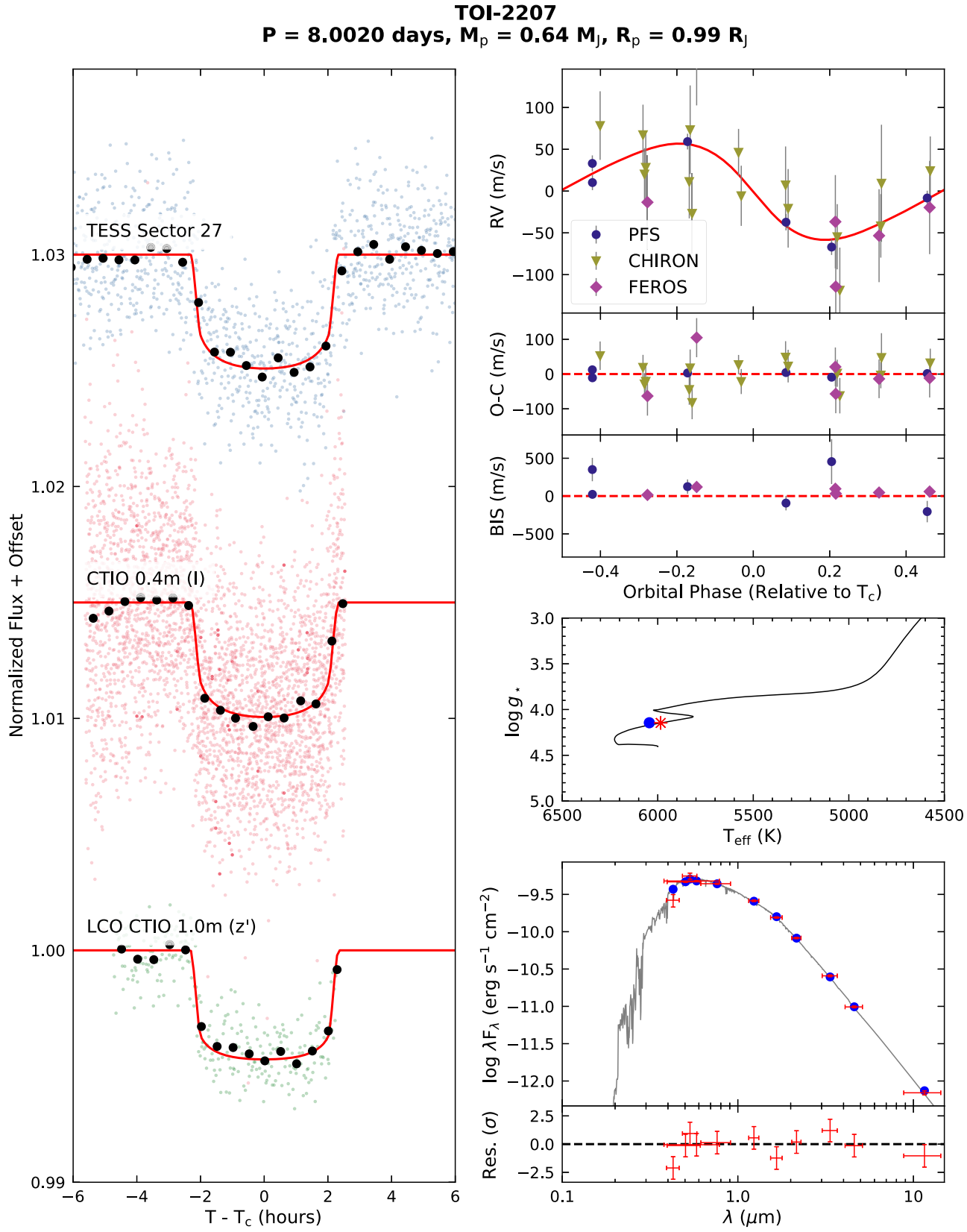

Figure 12. Same as Figure 6, but for TOI-2207 b.

$8\,R_\oplus < R_p < 24\,R_\oplus$). Our 10 planets orbit F and G stars, and all of the stars have metallicities similar to that of the Sun or higher, with a median [Fe/H] of $+0.18$. This is in line with the well-known preference for hot Jupiters to exist around stars with super-solar metallicities (Santos et al. 2004; Valenti & Fischer 2005).

The planets in our sample have masses and radii generally consistent with the previously known population of hot

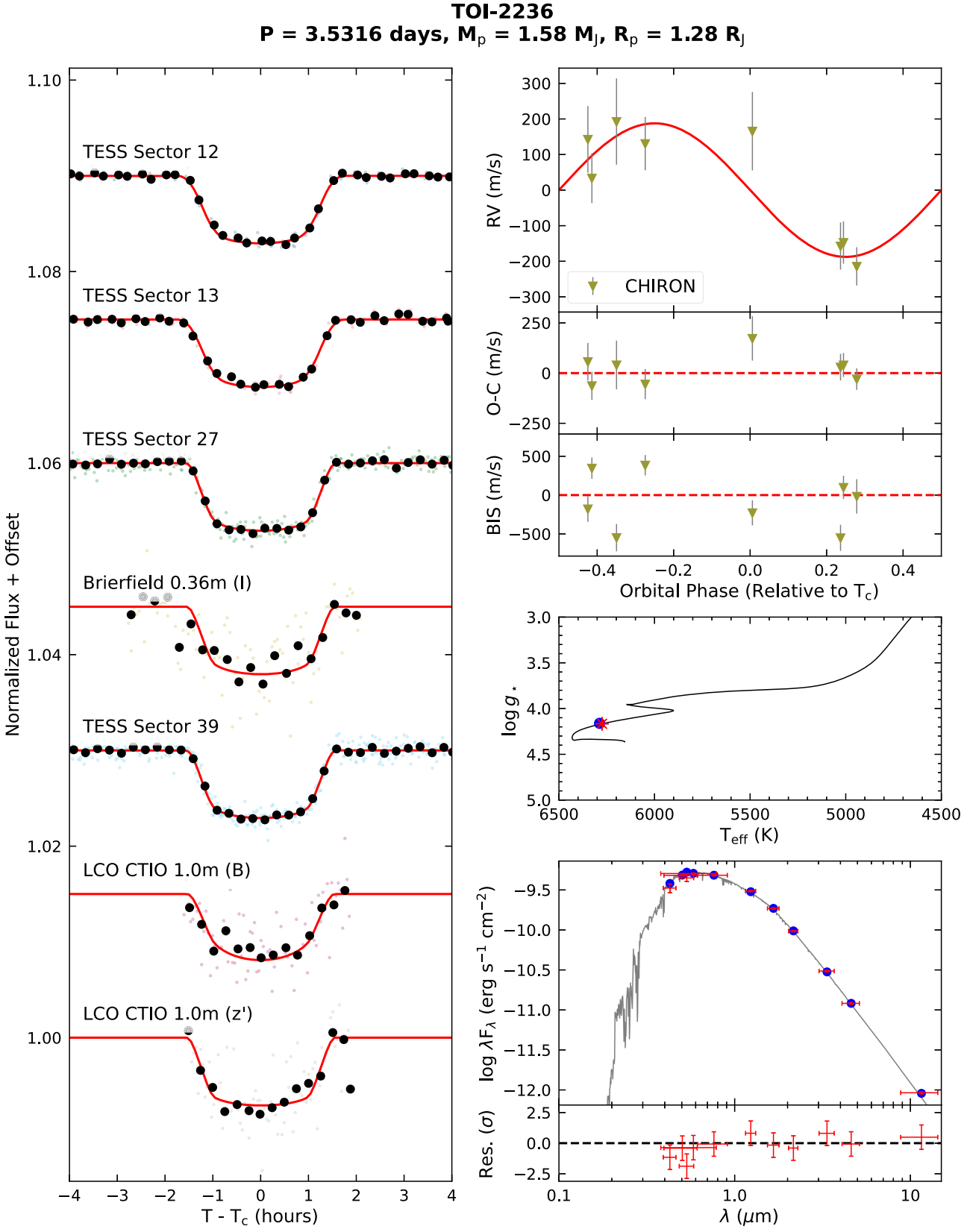

Figure 13. Same as Figure 6, but for TOI-2236 b.

Jupiters (Figure 8). The new planets are also consistent with the previously noted trend that hot Jupiters with higher incident fluxes tend to have larger radii (Figure 9; see also Demory & Seager 2011).

5.1. Two Inflated Saturns

Two of the host stars (TOI-2421, TOI-2567) appear to have recently evolved off the terminal age main sequence, with stellar radii $R_\star = 1.75 \pm 0.05\ R_\odot$ and $1.69 \pm 0.04\ R_\odot$, respectively. Their

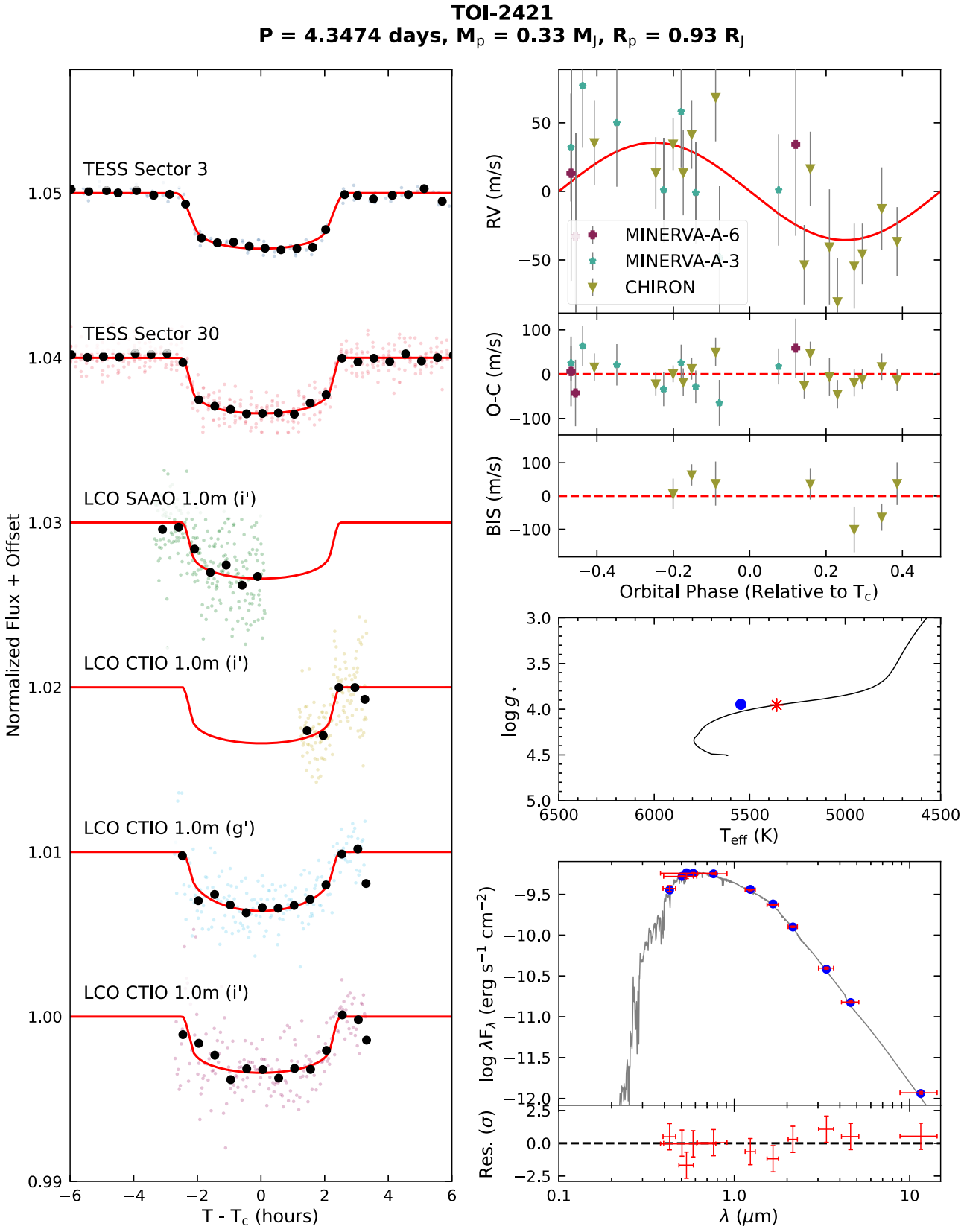

Figure 14. Same as Figure 6, but for TOI-2421 b.

masses are both about 1.13 $M_\odot$. These two stars also host the lowest-mass planets in our sample—TOI-2421b is a Saturn-mass planet, with a mass of $M_p = 0.33 \pm 0.08\,M_J$, and TOI-2567b is a sub-Saturn ($M_p = 0.20 \pm 0.03\,M_J$). The two planets lie on the upper boundary of the hot Neptune desert (Mazeh et al. 2016), as shown in the lower panel of Figure 9.

Both planets are inflated, with radii of $R_p = 0.925^{+0.035}_{-0.034} R_J$ and $0.975^{+0.031}_{-0.029} R_J$, respectively. Indeed, TOI-2567b has a bulk

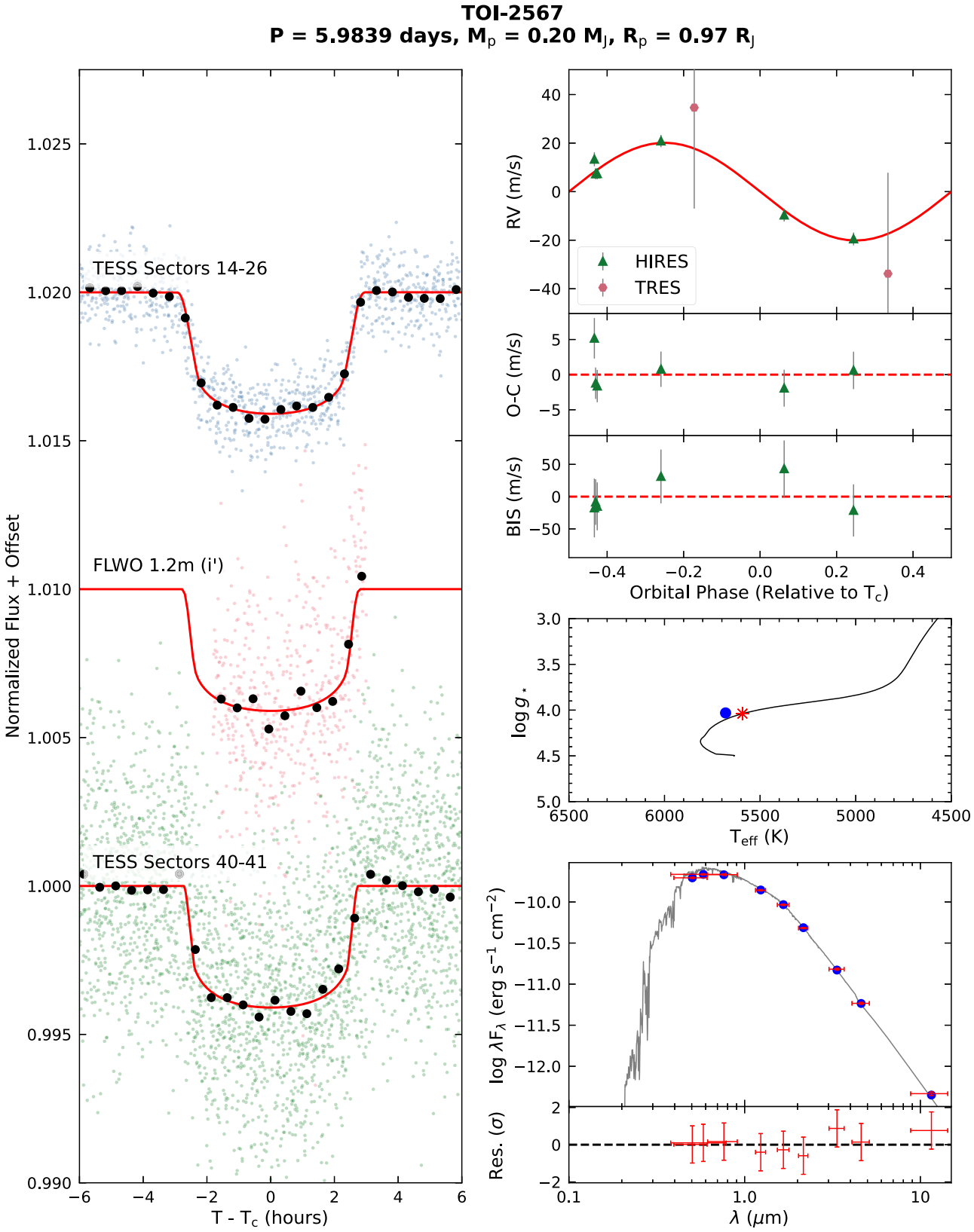

Figure 15. Same as Figure 6, but for TOI-2567 b.

density of just 0.27 ± 0.05 g cm^{-3}, making it one of the least dense planets known for its mass (Figure 10). The two planets join a small but growing collection of hot Saturns orbiting slightly evolved stars, including TOI-954 b (Sha et al. 2021), TOI-1296b (Moutou et al. 2021), and TOI-1842b (Wittenmyer et al. 2022). Such planets can help test models of radius reinflation around evolved stars (e.g., Lopez & Fortney 2016; Thorngren et al. 2021) by helping to place constraints on the timescale of reinflation, and via comparison with such trends for their more massive counterparts (e.g., Hartman et al. 2016).

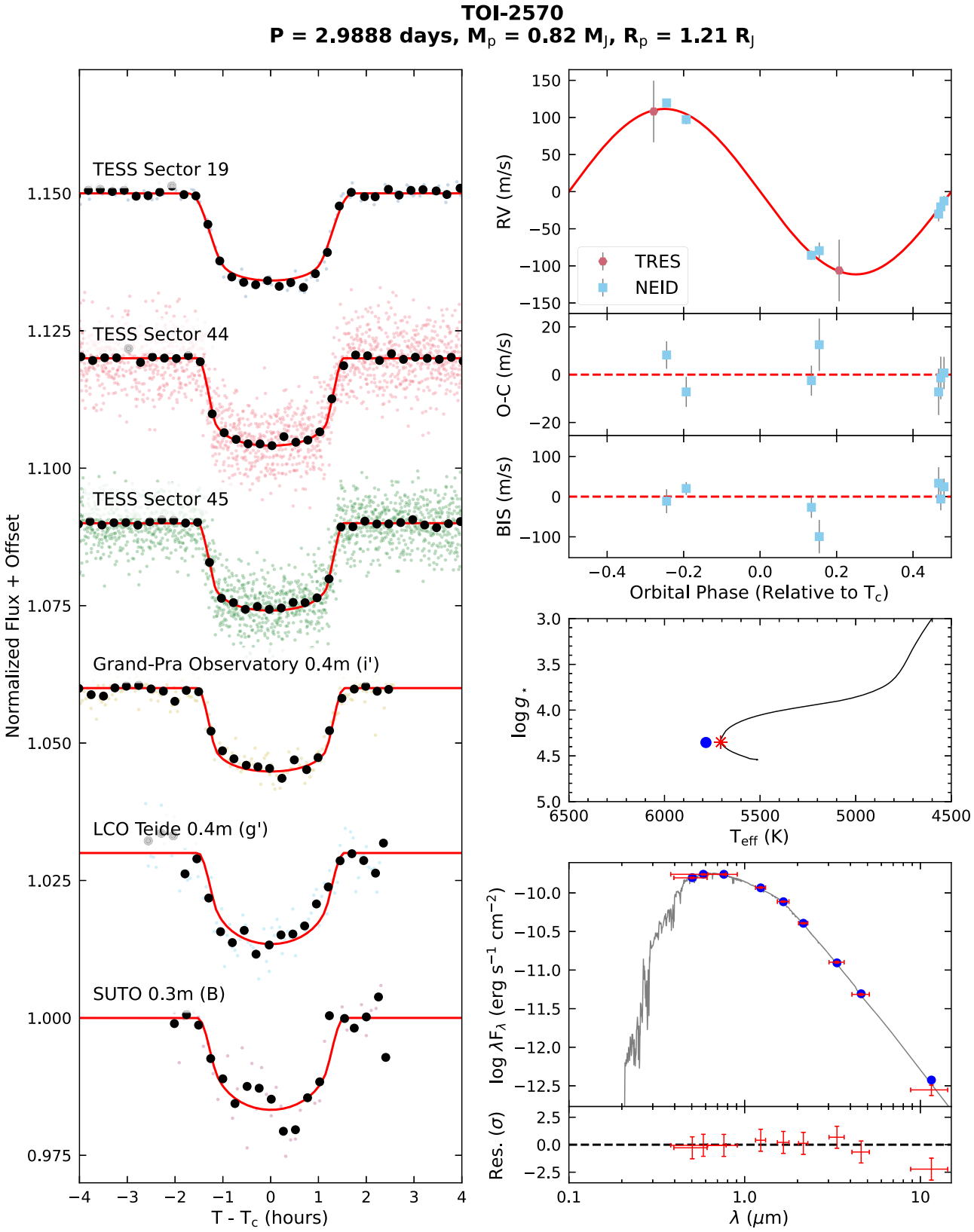

Figure 16. Same as Figure 6, but for TOI-2570 b.

5.2. Planet Eccentricities

While the shortest period hot Jupiters are expected to be on circular orbits due to tides raised by the star on the planet, the tidal circularization timescale increases rapidly with orbital distance. Tidal circularization might be too slow to have affected planets with periods approaching 10 days or longer, with an extreme example being the recently discovered TOI-3362b, a potential proto-hot Jupiter on a $P = 18.1$ day, $e = 0.82$

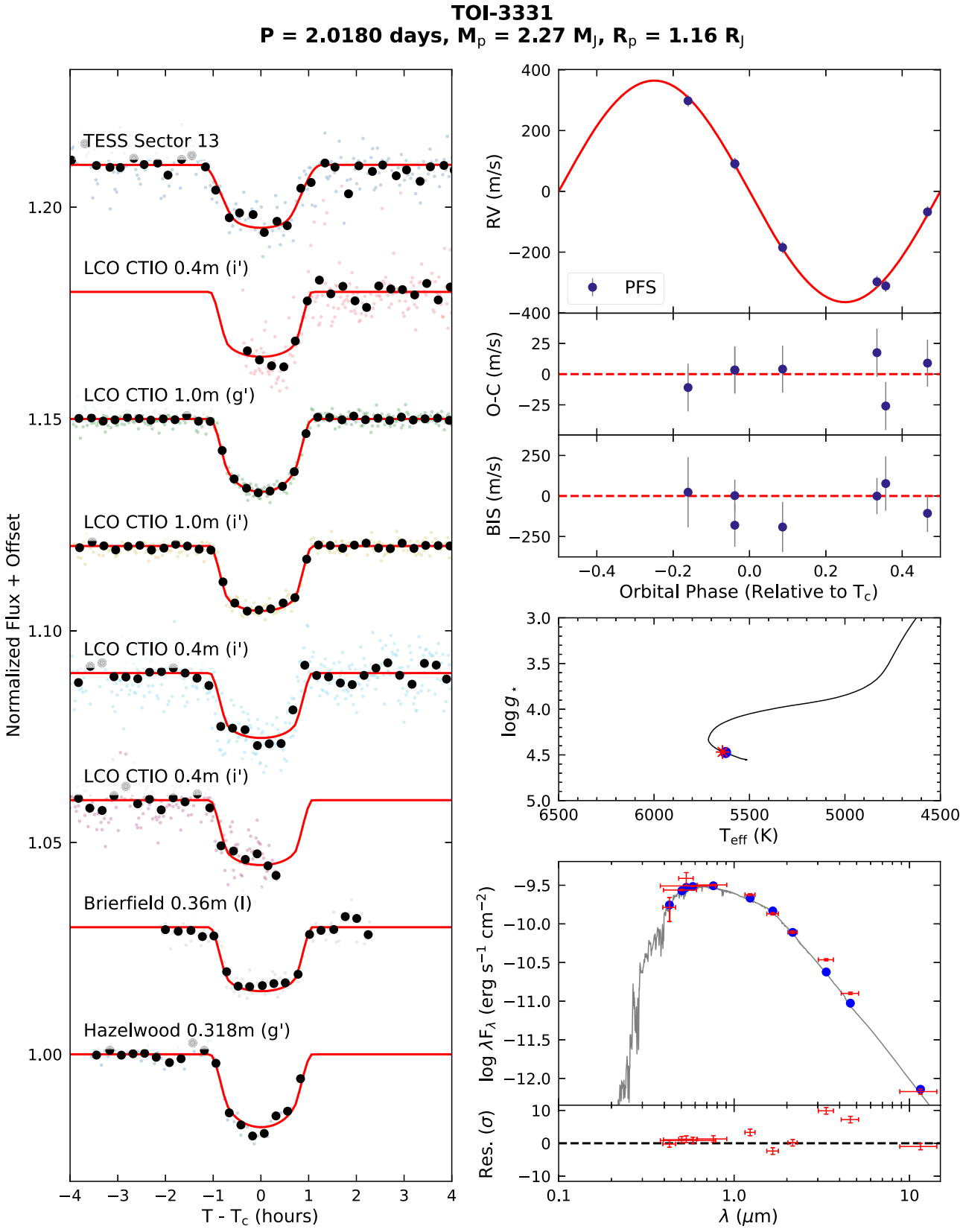

Figure 17. Same as Figure 6, but for TOI-3331 b.

orbit (Dong et al. 2021). Indeed, the two longest period planets in our sample, TOI-2207b ($P = 8.00$ days) and TOI-3693b ($P = 9.09$ days) have theoretical tidal circularization timescales of 12 ± 5 and 22 ± 6 Gyr, based on Equation (3) of Adams & Laughlin (2006), who extended the work of Goldreich & Soter (1966), and assuming a tidal quality factor of $Q_P = 10^6$.

The measured orbital eccentricity of TOI-2207b is $e = 0.174^{+0.048}_{-0.052}$, which is greater than zero by more than 3σ,

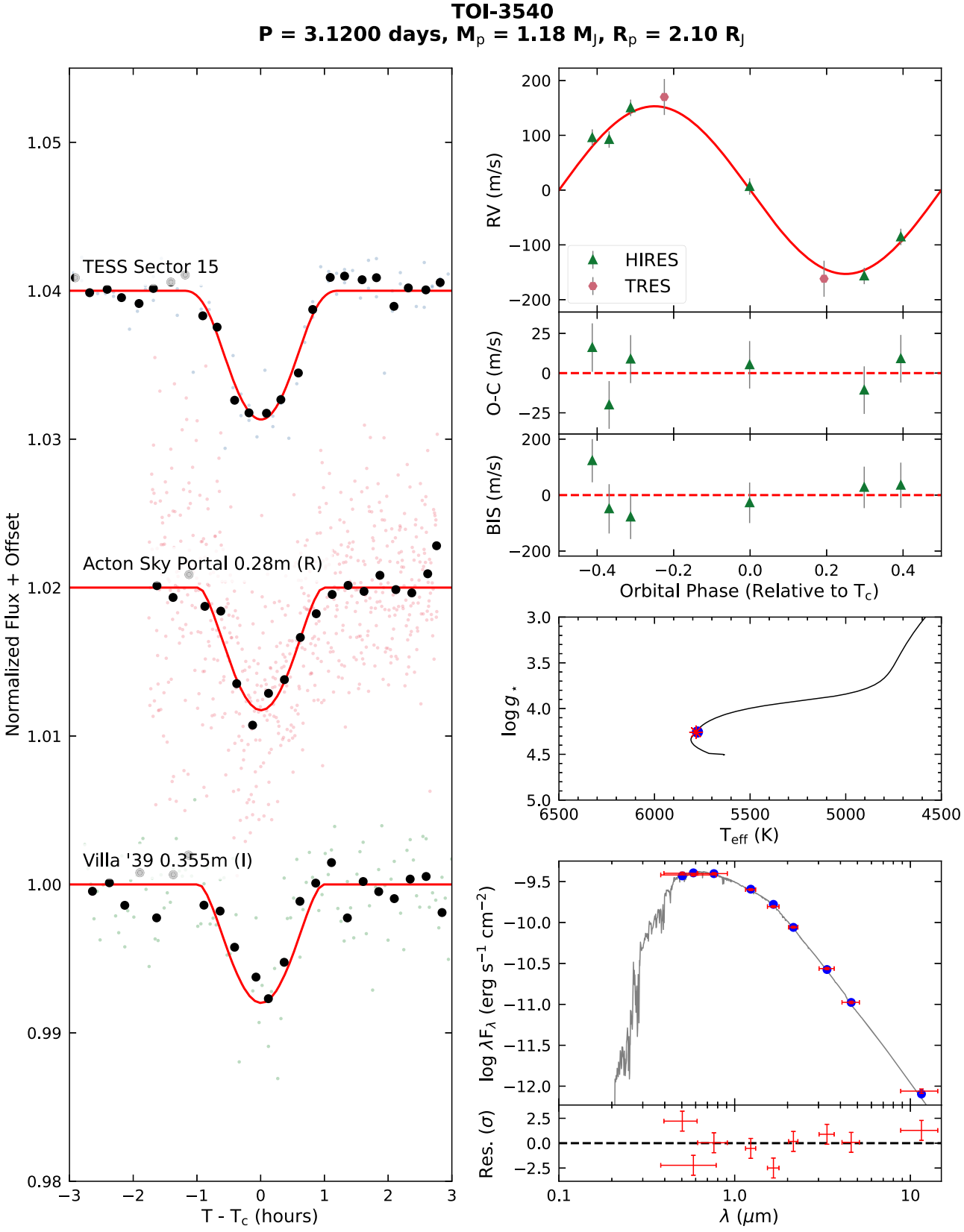

Figure 18. Same as Figure 6, but for TOI-3540 b.

although the significance of this result may be affected by the Lucy–Sweeney bias (Lucy & Sweeney 1971). Given that the estimated stellar age is 4 Gyr, which is of the same order of magnitude as the theoretical circularization timescale, the current eccentricity might be a remnant of a high-eccentricity migration formation pathway for this planet.

In contrast, TOI-3693b, which has a longer orbital period, appears to have a more circular orbit. The 68% and 95% upper

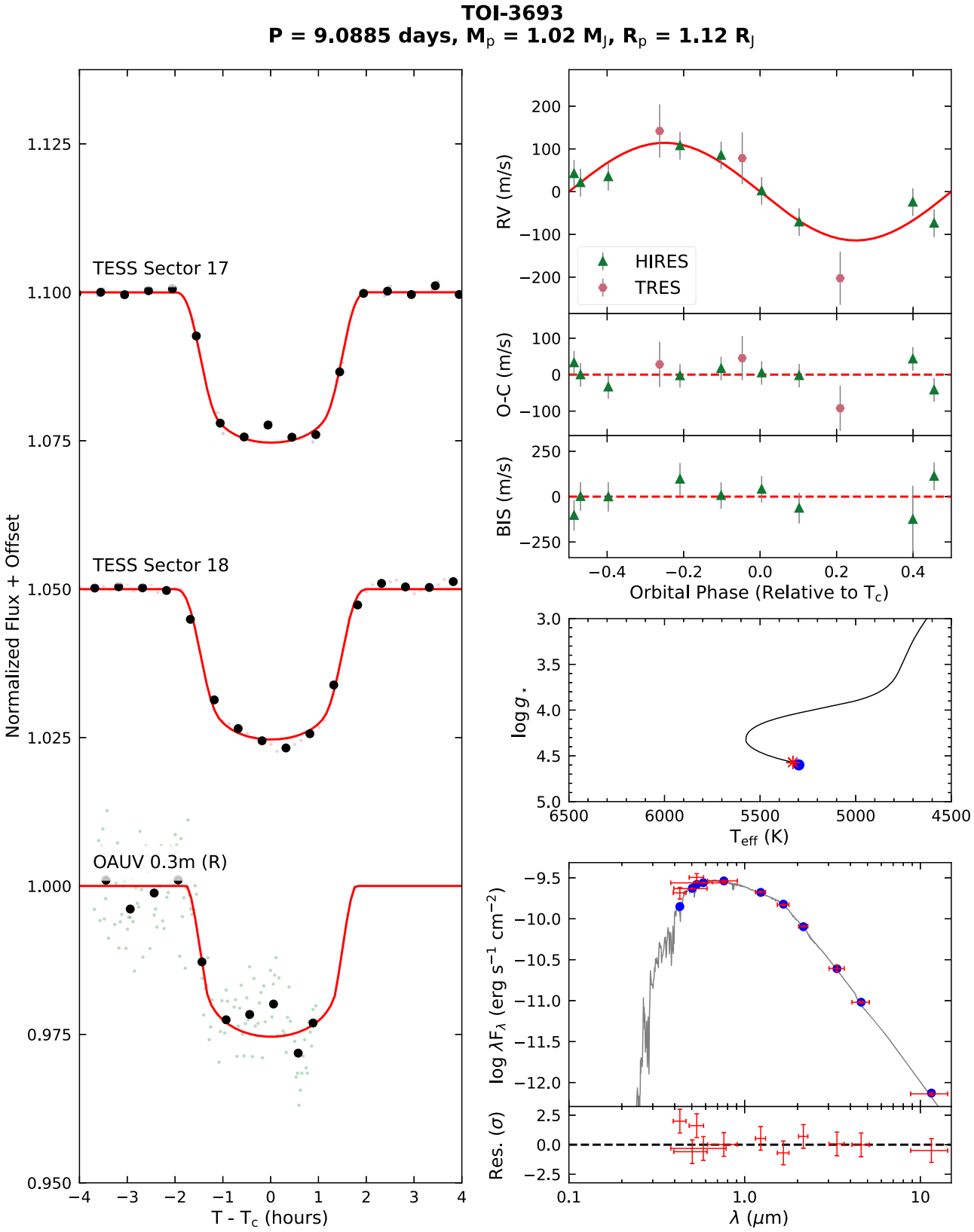

Figure 19. Same as Figure 6, but for TOI-3693 b.

limits for the eccentricity of this planet are $e < 0.054$ and $e < 0.13$, respectively. More data, including the possible timing and detection of a secondary eclipse, would be required to obtain a more secure measurement of the planet eccentricity, but TOI-3693b is not likely to have an orbital eccentricity similar to that of TOI-2207b or some other warm Jupiters (e.g., TOI-640 b, Rodriguez et al. 2021; TOI-559 b, Ikwut-Ukwa et al. 2021).

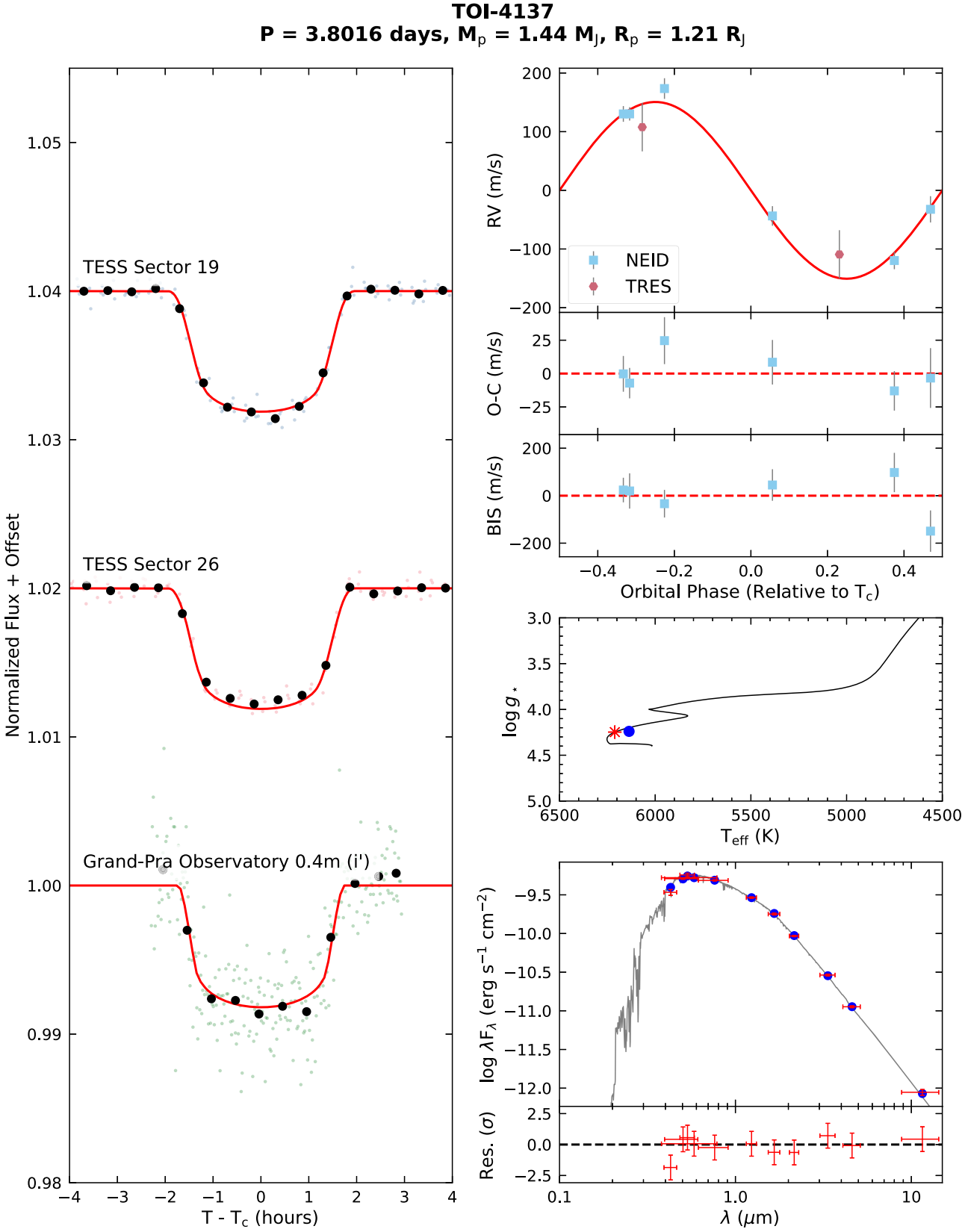

Figure 20. Same as Figure 6, but for TOI-4137 b.

These two longer period hot Jupiter systems are also potential targets for stellar obliquity measurements with the Rossiter–McLaughlin (RM) effect (Rossiter 1924; McLaughlin 1924). The expected RM amplitudes for the two systems are $\approx$30 m s^{-1} for TOI-2207b and $\approx$90 m s^{-1} for TOI-3693b (Gaudi & Winn 2007), which should be measurable on a large telescope given the relatively bright host stars ($V = 11.4$ and 12.0, respectively). The large planet-star separations of the two

planets ($a/R_\star \approx 12$ and 22, respectively) result in long tidal realignment timescales. Thus, misaligned orbits in these systems, particularly when correlated with orbital eccentricity, could be indicative of a high-eccentricity formation pathway, although they could also result from perturbations by an outer planets in the system.

6. Conclusions

We presented the discovery and characterization of 10 new hot Jupiters around F and G stars from NASA's TESS mission. These planets orbit relatively bright stars ($G < 12.5$) and are potential targets for atmospheric characterization, measurements of stellar obliquity, and other follow-up observations. While we have drawn attention to some of the notable features of the new planets, including the low density of the sub-Saturn TOI-2567b and the detectable eccentricity of TOI-2207b, the larger and longer-term purpose of the survey is to allow for more general conclusions to be drawn about the hot Jupiter population. This will require more observations to detect and confirm new planets (the "numerator" of demographic calculations) as well as a detailed examination of the TESS selection function and survey characteristics (the "denominator"). Based on the forecast of Yee et al. (2021), to assemble a sample of 400 hot Jupiters (an order of magnitude more planets than the Kepler sample), a magnitude-limited survey would need to be complete down to $G = 12.5$. The 10 planets described here, along with the other new TESS hot Jupiters that have been described in the literature (e.g., Rodriguez et al. 2019; Zhou et al. 2019; Brahm et al. 2020; Davis et al. 2020; Nielsen et al. 2020; Ikwut-Ukwa et al. 2021; Rodriguez et al. 2021; Sha et al. 2021; Wong et al. 2021; Knudstrup et al. 2022; Rodriguez et al. 2022) are steps toward realizing the promise of TESS for hot Jupiter demographics.

We thank the anonymous reviewer whose comments helped improve the manuscript. S.W.Y. thanks Gummi Stefansson for helpful conversations regarding the NEID observations.

This paper includes data collected by the TESS mission that are publicly available from the Mikulski Archive for Space Telescopes (MAST). Funding for the TESS mission is provided by NASA's Science Mission Directorate. We acknowledge the use of public TESS data from pipelines at the TESS Science Office and at the TESS Science Processing Operations Center. Resources supporting this work were provided by the NASA High-End Computing (HEC) Program through the NASA Advanced Supercomputing (NAS) Division at Ames Research Center for the production of the SPOC data products. We also acknowledge the use of data from the Exoplanet Follow-up Observation Program website, which is operated by the California Institute of Technology, under contract with the National Aeronautics and Space Administration under the Exoplanet Exploration Program. This research made use of Lightkurve, a Python package for Kepler and TESS data analysis (Lightkurve Collaboration et al. 2018).

Some of the data presented herein were obtained at the W. M. Keck Observatory, which is operated as a scientific partnership among the California Institute of Technology, the University of California and the National Aeronautics and Space Administration. The Observatory was made possible by the generous financial support of the W. M. Keck Foundation. Keck telescope time was granted by NOIRLab (Prop. ID 2021B-0162, PI: Yee) through the Mid-Scale Innovations Program (MSIP). MSIP is funded by NSF. The authors wish to recognize and acknowledge the very significant cultural role and reverence that the summit of Maunakea has always had within the indigenous Hawaiian community. We are most fortunate to have the opportunity to conduct observations from this mountain.

This paper contains data taken with the NEID instrument, which was funded by the NASA-NSF Exoplanet Observational Research (NN-EXPLORE) partnership and built by Pennsylvania State University. NEID is installed on the WIYN telescope, which is operated by the National Optical Astronomy Observatory, and the NEID archive is operated by the NASA Exoplanet Science Institute at the California Institute of Technology. NN-EXPLORE is managed by the Jet Propulsion Laboratory, California Institute of Technology under contract with the National Aeronautics and Space Administration. The data presented herein were obtained at the WIYN Observatory from telescope time allocated to NN-EXPLORE through the scientific partnership of the National Aeronautics and Space Administration, the National Science Foundation, and NOIRLab. This work was supported by a NASA WIYN PI Data Award, administered by the NASA Exoplanet Science Institute. The authors thank Sarah Logsdon and Heidi Schweiker for help with the NEID observations. The authors are honored to be permitted to conduct astronomical research on Iolkam Du'ag (Kitt Peak), a mountain with particular significance to the Tohono O'odham.

This paper includes data gathered with the 6.5 m Magellan Telescopes located at Las Campanas Observatory, Chile.

This research has used data from the CTIO/SMARTS 1.5 m telescope, which is operated as part of the SMARTS Consortium by RECONS (www.recons.org) members Todd Henry, Hodari James, Wei-Chun Jao, and Leonardo Paredes. At the telescope, observations were carried out by Roberto Aviles and Rodrigo Hinojosa. The CHIRON data were obtained from telescope time allocated under the NN-EXPLORE program with support from the National Aeronautics and Space Administration.

Some of the data presented herein were obtained at the MINERVA–Australis facility from telescope time allocated under the NN-EXPLORE program with support from the National Aeronautics and Space Administration. MINERVA–Australis is supported by Australian Research Council LIEF grant LE160100001, Discovery grants DP180100972 and DP220100365, Mount Cuba Astronomical Foundation, and institutional partners University of Southern Queensland, UNSW Sydney, MIT, Nanjing University, George Mason University, University of Louisville, University of California Riverside, University of Florida, and The University of Texas at Austin. We respectfully acknowledge the traditional custodians of all lands throughout Australia, and recognize their continued cultural and spiritual connection to the land, waterways, cosmos, and community. We pay our deepest respects to all Elders, ancestors and descendants of the Giabal, Jarowair, and Kambuwal nations, upon whose lands the MINERVA–Australis facility at Mt. Kent is situated.

This work makes use of observations from the LCOGT network. Part of the LCOGT telescope time was granted by NOIRLab through the Mid-Scale Innovations Program (MSIP). MSIP is funded by NSF.

This paper makes use of data from the MEarth Project, which is a collaboration between Harvard University and the Smithsonian Astrophysical Observatory. The MEarth Project

acknowledges funding from the David and Lucile Packard Fellowship for Science and Engineering, the National Science Foundation under grants AST-0807690, AST-1109468, AST-1616624 and AST-1004488 (Alan T. Waterman Award), the National Aeronautics and Space Administration under grant No. 80NSSC18K0476 issued through the XRP Program, and the John Templeton Foundation.

Adam Popowicz and Slawomir Lasota were responsible for data processing and automation of observations at SUTO observatories and were financed by grant BK-246/RAu-11/2022. A.J. acknowledges support from ANID—Millennium Science Initiative—ICN12_009 and FONDECYT project 1210718.

J.H. acknowledges support from NASA grants 80NSSC 19K0386, 80NSSC19K1728, and 80NSSC21K0335.

Facilities: TESS, MAST, Gaia, Keck: I (HIRES), WIYN (NEID), Magellan: Clay (PFS), CTIO: 1.5 m (CHIRON), Max Planck: 2.2 m (FEROS), FLWO: 1.5 m (TRES), LCOGT, Gemini.

Software: astropy (Astropy Collaboration et al. 2013, 2018), lightkurve (Lightkurve Collaboration et al. 2018), EXOFASTv2 (Eastman et al. 2019), SpecMatch-Emp (Yee et al. 2017), SpecMatch-Synth (Petigura 2015), AstroImageJ (Collins et al. 2017), TAPIR (Jensen 2013), numpy (Harris et al. 2020), scipy (Virtanen et al. 2020), pandas (pandas development team 2020; Wes McKinney 2010), matplotlib (Hunter 2007).

Appendix
Additional Fit Parameters

We present in Table 13 the median and 68% confidence intervals for additional fit parameters not listed in Table 12 for the adopted fits. These are the linear and quadratic limb-darkening parameters (u_1, u_2) in each band; additional flux dilution from neighboring stars in each band (D); the relative RV offset for each instrument $\gamma_{\rm rel}$ (m s^{-1}); and the RV jitter for each instrument σ_J (m s^{-1}).

Table 13
Additional Fit Parameters (Median and 68% Confidence Intervals)

Parameter					
TOI-2193					
	B	I	i′	z′	TESS
u_1	0.605 ± 0.035	$0.252^{+0.049}_{-0.050}$	$0.256^{+0.043}_{-0.044}$	0.211 ± 0.033	0.299 ± 0.031
u_2	0.192 ± 0.035	0.287 ± 0.049	0.275 ± 0.045	0.279 ± 0.033	0.310 ± 0.031
A_D	$0.00634^{+0.00064}_{-0.00063}$	0.0312 ± 0.0031	0.0273 ± 0.0028	0.0366 ± 0.0037	0.0004 ± 0.0034
	PFS				
$\gamma_{\rm rel}$	25 ± 15				
σ_J	37^{+20}_{-11}				
TOI-2207					
	I	z′	TESS		
u_1	0.247 ± 0.044	0.164 ± 0.044	0.261 ± 0.045		
u_2	0.304 ± 0.047	$0.265^{+0.047}_{-0.048}$	0.305 ± 0.048		
A_D	⋯	–-	-0.0000 ± 0.0029		
	CHIRON	FEROS	PFS		
$\gamma_{\rm rel}$	-35056 ± 11	-35676 ± 40	$-10.8^{+8.0}_{-8.1}$		
σ_J	10^{+21}_{-11}	92^{+65}_{-31}	$17.4^{+15}_{-7.7}$		
TOI-2236					
	B	I	z′	TESS	
u_1	0.549 ± 0.052	0.227 ± 0.050	0.192 ± 0.050	0.232 ± 0.025	
u_2	0.219 ± 0.051	$0.306^{+0.050}_{-0.049}$	$0.302^{+0.050}_{-0.049}$	0.302 ± 0.025	
A_D	⋯	–-	⋯	-0.0008 ± 0.0046	
	CHIRON				
$\gamma_{\rm rel}$	45127^{+40}_{-35}				
σ_J	58^{+70}_{-58}				
TOI-2421					
	g′	i′	TESS		
u_1	$0.615^{+0.051}_{-0.052}$	0.349 ± 0.031	0.327 ± 0.033		
u_2	0.146 ± 0.051	0.277 ± 0.029	0.260 ± 0.035		
A_D	⋯	–-	$-0.000000^{+0.00010}_{-0.000100}$		
	CHIRON	MINERVA-A-3	MINERVA-A-6		
$\gamma_{\rm rel}$	$6432.2^{+7.8}_{-7.6}$	7020 ± 19	7110^{+160}_{-170}		
σ_J	$8.3^{+17}_{-8.3}$	41^{+27}_{-17}	260^{+400}_{-180}		
TOI-2567					
	i′	TESS			
u_1	$0.346^{+0.049}_{-0.050}$	$0.329^{+0.031}_{-0.032}$			
u_2	0.271 ± 0.050	0.259 ± 0.035			
A_D	⋯	0.0009 ± 0.0088			
	HIRES				

Table 13
(Continued)

Parameter				
$\gamma_{\rm rel}$	$-3.2^{+2.2}_{-2.0}$			
σ_J	$3.8^{+5.1}_{-2.9}$			
TOI-2570				
	B	g′	i′	TESS
u_1	$0.677^{+0.055}_{-0.056}$	0.589 ± 0.053	0.309 ± 0.044	0.299 ± 0.028
u_2	0.141 ± 0.053	0.186 ± 0.052	0.264 ± 0.047	0.273 ± 0.029
A_D	⋯	−-	⋯	-0.062 ± 0.016
	NEID			
$\gamma_{\rm rel}$	-45135.4 ± 5.0			
σ_J	$10.0^{+9.0}_{-4.9}$			
TOI-3331				
	I	g′	i′	TESS
u_1	0.303 ± 0.050	$0.639^{+0.040}_{-0.041}$	0.343 ± 0.028	0.324 ± 0.051
u_2	0.249 ± 0.049	0.178 ± 0.040	0.263 ± 0.026	0.251 ± 0.050
A_D	0.123 ± 0.011	0.0506 ± 0.0053	$0.1159^{+0.0097}_{-0.0098}$	0.107 ± 0.039
	PFS			
$\gamma_{\rm rel}$	66 ± 13			
σ_J	27^{+28}_{-11}			
TOI-3540				
	I	R	TESS	
u_1	$0.329^{+0.050}_{-0.051}$	$0.370^{+0.049}_{-0.050}$	$0.268^{+0.048}_{-0.049}$	
u_2	0.317 ± 0.050	0.281 ± 0.049	$0.248^{+0.048}_{-0.049}$	
A_D	0.167 ± 0.016	0.143 ± 0.014	0.151 ± 0.015	
	HIRES			
$\gamma_{\rm rel}$	-19 ± 12			
σ_J	$25^{+25}_{-10.}$			
TOI-3693				
	R	TESS		
u_1	0.406 ± 0.051	0.367 ± 0.035		
u_2	$0.197^{+0.051}_{-0.052}$	0.238 ± 0.036		
A_D	⋯	-0.0045 ± 0.0098		
	HIRES	TRES		
$\gamma_{\rm rel}$	-13 ± 13	197^{+93}_{-91}		
σ_J	$36.4^{+16}_{-9.8}$	164^{+96}_{-79}		
TOI-4137				
	i′	TESS		
u_1	0.251 ± 0.048	0.237 ± 0.033		
u_2	0.315 ± 0.049	0.293 ± 0.034		
A_D	⋯	0.007 ± 0.011		
	NEID			
$\gamma_{\rm rel}$	-41121^{+13}_{-11}			
σ_J	19^{+27}_{-19}			

Note. These value and the results form the fits where the eccentricity was allowed to float are available in the machine-readable version of Table 12.

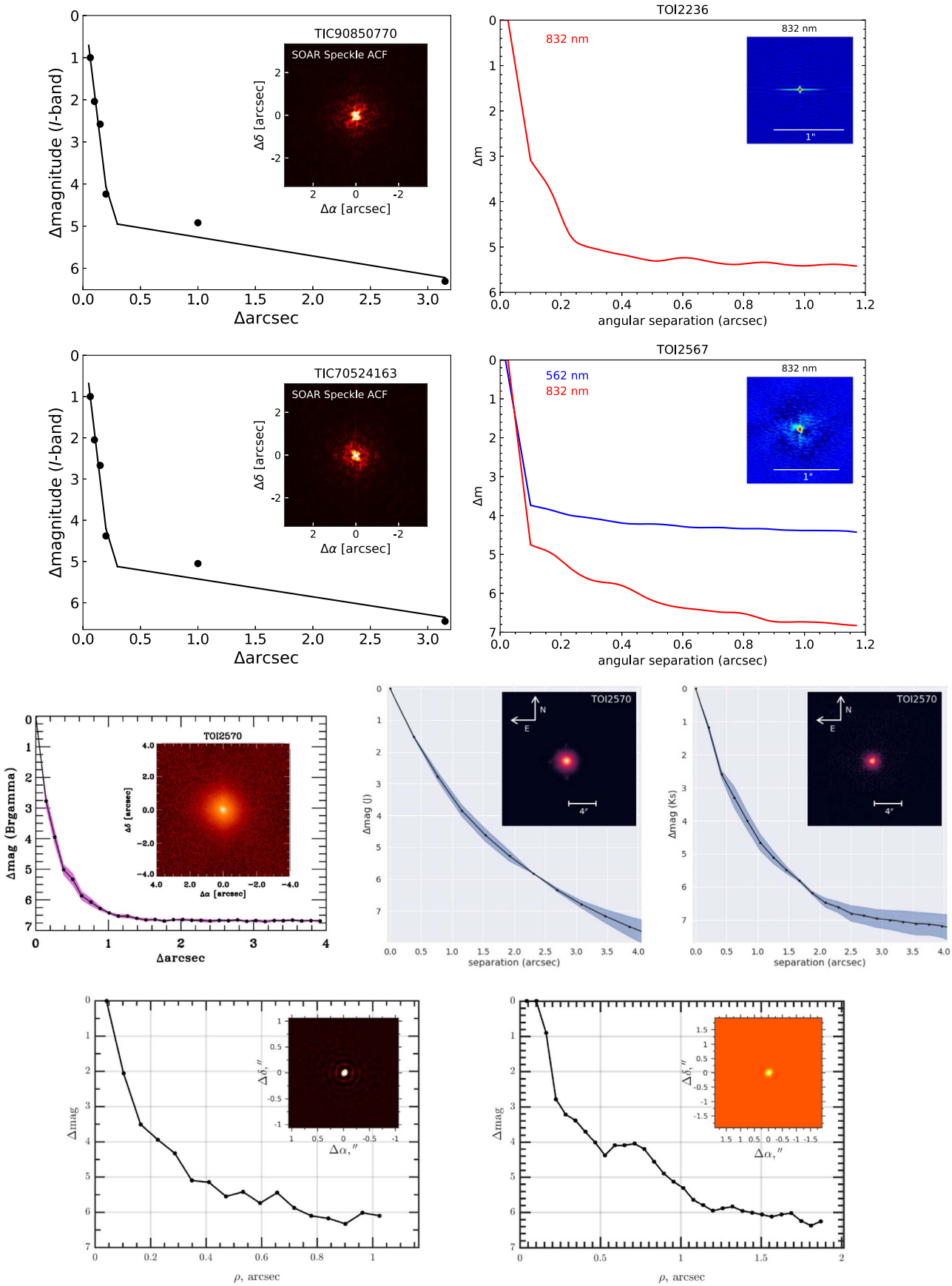

Figure 21. High-resolution imaging of hot Jupiter hosts described in this paper. From top to bottom, left to right: Row 1: SOAR HRCam Observation of TOI-2207; Gemini-South Zorro Observation of TOI-2236; Row 2: SOAR HRCam Observation of TOI-2374; SOAR HRCam Observation of TOI-2421; Row 3: Gemini-North 'Alopeke Observation of TOI-2567; ShaneAO/SHARCS Observation (J band) of TOI-2570; ShaneAO/SHARCS Observation (K_s band) of TOI-2570; Row 4: SAI-2.5 m Speckle Polarimeter Observation of TOI-3693; SAI-2.5 m Speckle Polarimeter Observation of TOI-4137. No companions were detected down to the instrumental detection limits for any of these targets.

ORCID iDs

Samuel W. Yee https://orcid.org/0000-0001-7961-3907
Joshua N. Winn https://orcid.org/0000-0002-4265-047X
Joel D. Hartman https://orcid.org/0000-0001-8732-6166
Joseph E. Rodriguez https://orcid.org/0000-0001-8812-0565
George Zhou https://orcid.org/0000-0002-4891-3517
Samuel N. Quinn https://orcid.org/0000-0002-8964-8377
David W. Latham https://orcid.org/0000-0001-9911-7388
Allyson Bieryla https://orcid.org/0000-0001-6637-5401
Karen A. Collins https://orcid.org/0000-0001-6588-9574
Brett C. Addison https://orcid.org/0000-0003-3216-0626
Isabel Angelo https://orcid.org/0000-0002-9751-2664
Khalid Barkaoui https://orcid.org/0000-0003-1464-9276
Paul Benni https://orcid.org/0000-0001-6981-8722
Andrew W. Boyle https://orcid.org/0000-0001-6037-2971
Rafael Brahm https://orcid.org/0000-0002-9158-7315
R. Paul Butler https://orcid.org/0000-0003-1305-3761
David R. Ciardi https://orcid.org/0000-0002-5741-3047
Kevin I. Collins https://orcid.org/0000-0003-2781-3207
Dennis M. Conti https://orcid.org/0000-0003-2239-0567
Jeffrey D. Crane https://orcid.org/0000-0002-5226-787X
Fei Dai https://orcid.org/0000-0002-8958-0683
Courtney D. Dressing https://orcid.org/0000-0001-8189-0233
Jason D. Eastman https://orcid.org/0000-0003-3773-5142
Zahra Essack https://orcid.org/0000-0002-2482-0180
Raquel Forés-Toribio https://orcid.org/0000-0002-6482-2180
Elise Furlan https://orcid.org/0000-0001-9800-6248
Tianjun Gan https://orcid.org/0000-0002-4503-9705
Steven Giacalone https://orcid.org/0000-0002-8965-3969
Holden Gill https://orcid.org/0000-0001-6171-7951
Eric Girardin https://orcid.org/0000-0002-5443-3640
Thomas Henning https://orcid.org/0000-0002-1493-300X
Christopher E. Henze https://orcid.org/0000-0003-3216-0626
Melissa J. Hobson https://orcid.org/0000-0002-5945-7975
Jonathan Horner https://orcid.org/0000-0002-1160-7970
Andrew W. Howard https://orcid.org/0000-0001-8638-0320
Steve B. Howell https://orcid.org/0000-0002-2532-2853
Chelsea X. Huang https://orcid.org/0000-0003-0918-7484
Howard Isaacson https://orcid.org/0000-0002-0531-1073
Jon M. Jenkins https://orcid.org/0000-0002-4715-9460
Eric L. N. Jensen https://orcid.org/0000-0002-4625-7333
Andrés Jordán https://orcid.org/0000-0002-5389-3944
Stephen R. Kane https://orcid.org/0000-0002-7084-0529
John F. Kielkopf https://orcid.org/0000-0003-0497-2651
Slawomir Lasota https://orcid.org/0000-0002-7830-6822
Alan M. Levine https://orcid.org/0000-0001-8172-0453
Jack Lubin https://orcid.org/0000-0001-8342-7736
Andrew W. Mann https://orcid.org/0000-0003-3654-1602
Bob Massey https://orcid.org/0000-0001-8879-7138
Kim K. McLeod https://orcid.org/0000-0001-9504-1486
Matthew W. Mengel https://orcid.org/0000-0002-7830-6822
Jose A. Muñoz https://orcid.org/0000-0001-9833-2959
Felipe Murgas https://orcid.org/0000-0001-9087-1245
Enric Palle https://orcid.org/0000-0003-0987-1593
Peter Plavchan https://orcid.org/0000-0002-8864-1667
Adam Popowicz https://orcid.org/0000-0003-3184-5228
Don J. Radford https://orcid.org/0000-0002-3940-2360
George R. Ricker https://orcid.org/0000-0003-2058-6662
Pamela Rowden https://orcid.org/0000-0002-4829-7101
Boris S. Safonov https://orcid.org/0000-0003-1713-3208
Arjun B. Savel https://orcid.org/0000-0002-2454-768X
Richard P. Schwarz https://orcid.org/0000-0001-8227-1020
S. Seager https://orcid.org/0000-0002-3940-2360
Avi Shporer https://orcid.org/0000-0002-1836-3120
C. G. Tinney https://orcid.org/0000-0002-7595-0970
Dakotah Tyler https://orcid.org/0000-0003-0298-4667
Robert A. Wittenmyer https://orcid.org/0000-0001-9957-9304
Hui Zhang https://orcid.org/0000-0003-3491-6394
Carl Ziegler https://orcid.org/0000-0002-0619-7639

References

Adams, F. C., & Laughlin, G. 2006, ApJ, 649, 1004
Addison, B. C., Wright, D. J., Nicholson, B. A., et al. 2021, MNRAS, 502, 3704
Addison, B., Wright, D. J., Wittenmyer, R. A., et al. 2019, PASP, 131, 115003
Agol, E., Luger, R., & Foreman-Mackey, D. 2020, AJ, 159, 123
Alonso, R., Brown, T. M., Torres, G., et al. 2004, ApJ, 613, L153
Astropy Collaboration, Robitaille, T. P., Tollerud, E. J., et al. 2013, A&A, 558, A33
Astropy Collaboration, Price-Whelan, A. M., Sipőcz, B. M., et al. 2018, AJ, 156, 123
Bakos, G. Á., Csubry, Z., Penev, K., et al. 2013, PASP, 125, 154
Bakos, G., Noyes, R. W., Kovács, G., et al. 2004, PASP, 116, 266
Baranne, A., Queloz, D., Mayor, M., et al. 1996, A&AS, 119, 373
Berta, Z. K., Irwin, J., Charbonneau, D., Burke, C. J., & Falco, E. E. 2012, AJ, 144, 145
Brahm, R., Espinoza, N., Jordán, A., et al. 2019, AJ, 158, 45
Brahm, R., Jordán, A., & Espinoza, N. 2017, PASP, 129, 034002
Brahm, R., Nielsen, L. D., Wittenmyer, R. A., et al. 2020, AJ, 160, 235
Brown, A. G. A., Vallenari, A., Prusti, T., et al. 2021, A&A, 649, A1
Brown, T. M., Baliber, N., Bianco, F. B., et al. 2013, PASP, 125, 1031
Buchhave, L. A., Bakos, G. Á., Hartman, J. D., et al. 2010, ApJ, 720, 1118
Buchhave, L. A., Latham, D. W., Johansen, A., et al. 2012, Natur, 486, 375
Butler, R. P., Marcy, G. W., Williams, E., et al. 1996, PASP, 108, 500
Caldwell, D. A., Tenenbaum, P., Twicken, J. D., et al. 2020, RNAAS, 4, 201
Choi, J., Dotter, A., Conroy, C., et al. 2016, ApJ, 823, 102
Claret, A. 2017, A&A, 600, A30
Claret, A., & Bloemen, S. 2011, A&A, 529, A75
Carter, J. A., & Agol, E. 2013, ApJ, 765, 132
Coelho, P., Barbuy, B., Meléndez, J., Schiavon, R. P., & Castilho, B. V. 2005, A&A, 443, 735
Collins, K., Quinn, S. N., Latham, D. W., et al. 2018, AAS Meeting Abstracts, 231, 439.08
Collins, K. A., Kielkopf, J. F., Stassun, K. G., & Hessman, F. V. 2017, AJ, 153, 77
Collins, K. A., Collins, K. I., Pepper, J., et al. 2018, AJ, 156, 234
Crane, J. D., Shectman, S. A., & Butler, R. P. 2006, Proc. SPIE, 6269, 626931
Crane, J. D., Shectman, S. A., Butler, R. P., et al. 2010, Proc. SPIE, 7735, 773553
Crane, J. D., Shectman, S. A., Butler, R. P., Thompson, I. B., & Burley, G. S. 2008, Proc. SPIE, 7014, 701479
Cutri, R. M. 2012, VizieR Online Data Catalog, II/311
Cutri, R. M., Skrutskie, M. F., van Dyk, S., et al. 2003, VizieR Online Data Catalog, II/246
Dalba, P. A., Fulton, B., Isaacson, H., Kane, S. R., & Howard, A. W. 2020, AJ, 160, 149
Davis, A. B., Wang, S., Jones, M., et al. 2020, AJ, 160, 229
Dawson, R. I., & Johnson, J. A. 2018, ARA&A, 56, 175
Demory, B.-O., & Seager, S. 2011, ApJS, 197, 12
Donati, J.-F., Semel, M., Carter, B. D., Rees, D. E., & Cameron, A. C. 1997, MNRAS, 291, 658
Dong, J., Huang, C. X., Zhou, G., et al. 2021, ApJL, 920, L16
Dotter, A. 2016, ApJS, 222, 8
Eastman, J., Gaudi, B. S., & Agol, E. 2013, PASP, 125, 83
Eastman, J. D., Rodriguez, J. E., Agol, E., et al. 2019, arXiv:1907.09480
ExoFOP 2019, Exoplanet Follow-up Observing Program -TESS, IPAC, https://catcopy.ipac.caltech.edu/dois/doi.php?id=10.26134/EXOFOP3
Fabrycky, D., & Tremaine, S. 2007, ApJ, 669, 1298
Fausnaugh, M. M., Burke, C. J., Ricker, G. R., & Vanderspek, R. 2020, RNAAS, 4, 251
Feinstein, A. D., Montet, B. T., Foreman-Mackey, D., et al. 2019, PASP, 131, 094502
Fűrész, G. 2008, PhD thesis, University of Szeged, Hungary

Fortney, J. J., Dawson, R. I., & Komacek, T. D. 2021, JGRE, 126, e2020JE006629
Gaudi, B. S., & Winn, J. N. 2007, ApJ, 655, 550
Gavel, D., Kupke, R., Dillon, D., et al. 2014, Proc. SPIE, 9148, 38
Gelman, A., & Rubin, D. B. 1992, StaSc, 7, 457
Goldreich, P., & Soter, S. 1966, Icar, 5, 375
Guerrero, N. M., Seager, S., Huang, C. X., et al. 2021, ApJS, 254, 39
Halverson, S., Terrien, R., Mahadevan, S., et al. 2016, Proc. SPIE, 9908, 99086P
Harris, C. R., Millman, K. J., van der Walt, S. J., et al. 2020, Natur, 585, 357
Hartman, J. D., Bakos, G. Á., Bayliss, D., et al. 2019, AJ, 157, 55
Hartman, J. D., Bakos, G. Á., Bhatti, W., et al. 2016, AJ, 152, 182
Hayward, T. L., Brandl, B., Pirger, B., et al. 2001, PASP, 113, 105
Høg, E., Fabricius, C., Makarov, V. V., et al. 2000, A&A, 355, L27
Horch, E. P., Howell, S. B., Everett, M. E., & Ciardi, D. R. 2014, ApJ, 795, 60
Howard, A. W., & Fulton, B. J. 2016, PASP, 128, 114401
Howard, A. W., Johnson, J. A., Marcy, G. W., et al. 2010, ApJ, 721, 1467
Huang, C. X., Vanderburg, A., Pál, A., et al. 2020a, RNAAS, 4, 204
Huang, C. X., Vanderburg, A., Pál, A., et al. 2020b, RNAAS, 4, 206
Hunter, J. D. 2007, Computing in Science Engineering, 9, 90
Ikwut-Ukwa, M., Rodriguez, J. E., Quinn, S. N., et al. 2021, AJ, 163, 9
Irwin, J., Irwin, M., Aigrain, S., et al. 2007, MNRAS, 375, 1449
Jenkins, J. M., Twicken, J. D., McCauliff, S., et al. 2016, Proc. SPIE, 9913, 99133E
Jensen, E. 2013, Tapir: A web interface for transit/eclipse observability, Astrophysics Source Code Library, ascl:1306.007
Kaufer, A., Stahl, O., Tubbesing, S., et al. 1999, Msngr, 95, 8
Knudstrup, E., Serrano, L. M., Gandolfi, D., et al. 2022, arXiv:2204.13956
Kostov, V. B., Mullally, S. E., Quintana, E. V., et al. 2019, AJ, 157, 124
Kovács, G., Zucker, S., & Mazeh, T. 2002, A&A, 391, 369
Kruse, E., Agol, E., Luger, R., & Foreman-Mackey, D. 2019, ApJS, 244, 11
Kunimoto, M., Daylan, T., Guerrero, N., et al. 2022, ApJS, 259, 33
Kunimoto, M., Huang, C., Tey, E., et al. 2021, RNAAS, 5, 234
Kupke, R., Gavel, D., Roskosi, C., et al. 2012, Proc. SPIE, 8447, 88473G
Kurucz, R. L. 1993, SYNTHE Spectrum Synthesis Programs and Line Data
Lightkurve Collaboration, Cardoso, J. V. D. M., Hedges, C., et al. 2018, Lightkurve: Kepler and TESS time series analysis in Python Astrophysics Source Code Library, ascl:1812.013
Lin, D. N. C., & Papaloizou, J. 1986, ApJ, 309, 846
Lindegren, L., Klioner, S. A., Hernández, J., et al. 2021, A&A, 649, A2
Lopez, E. D., & Fortney, J. J. 2016, ApJ, 818, 4
Lucy, L. B., & Sweeney, M. A. 1971, AJ, 76, 544
Mandel, K., & Agol, E. 2002, ApJL, 580, L171
Matson, R. A., Howell, S. B., Horch, E. P., & Everett, M. E. 2018, AJ, 156, 31
Mayor, M., & Queloz, D. 1995, Natur, 378, 355
Mazeh, T., Holczer, T., & Faigler, S. 2016, A&A, 589, A75
McCullough, P. R., Stys, J. E., Valenti, J. A., et al. 2005, PASP, 117, 783
McGurk, R., Rockosi, C., Gavel, D., et al. 2014, Proc. SPIE, 9148, 91483A
McLaughlin, D. B. 1924, ApJ, 60, 22
Mireles, I., Hesse, K., Guerrero, N., et al. 2021, Posters from the TESS Science Conference II (TSC2), 128
Montalto, M., Borsato, L., Granata, V., et al. 2020, MNRAS, 498, 1726
Morton, T. D. 2015, isochrones: Stellar model grid package, Astrophysics Source Code Library, ascl:1503.010
Moutou, C., Almenara, J. M., Hébrard, G., et al. 2021, A&A, 653, A147
NASA Exoplanet Archive 2022, Planetary Systems Composite Parameters, v2022-02-14, NExScI-Caltech/IPAC, doi:10.26133/NEA13
Nielsen, L. D., Bouchy, F., Turner, O., et al. 2019, A&A, 623, A100
Nielsen, L. D., Brahm, R., Bouchy, F., et al. 2020, A&A, 639, A76
Nutzman, P., & Charbonneau, D. 2008, PASP, 120, 317
Olmschenk, G., Silva, S. I., Rau, G., et al. 2021, AJ, 161, 273
pandas development team, T. 2020, pandas-dev/pandas: Pandas, vlatest, Zenodo, doi:10.5281/zenodo.3509134
Paredes, L. A., Henry, T. J., Quinn, S. N., et al. 2021, AJ, 162, 176
Pepe, F., Mayor, M., Galland, F., et al. 2002, A&A, 388, 632
Pepper, J., Kuhn, R. B., Siverd, R., James, D., & Stassun, K. 2012, PASP, 124, 230
Pepper, J., Pogge, R. W., DePoy, D. L., et al. 2007, PASP, 119, 923
Petigura, E. A. 2015, PhD thesis, University of California, Berkeley, United States
Pollacco, D. L., Skillen, I., Cameron, A. C., et al. 2006, PASP, 118, 1407
Quinn, S. N., White, R. J., Latham, D. W., et al. 2012, ApJ, 756, L33
Rasio, F. A., & Ford, E. B. 1996, Sci, 274, 954
Ricker, G. R., Winn, J. N., Vanderspek, R., et al. 2015, JATIS, 1, 014003
Riello, M., Angeli, F. D., Evans, D. W., et al. 2021, A&A, 649, A3
Rodriguez, J. E., Quinn, S. N., Huang, C. X., et al. 2019, AJ, 157, 191
Rodriguez, J. E., Quinn, S. N., Zhou, G., et al. 2021, AJ, 161, 194
Rodriguez, J. E., Quinn, S. N., Vanderburg, A., et al. 2022, arXiv:2205.05709
Rossiter, R. A. 1924, ApJ, 60, 15
Safonov, B. S., Lysenko, P. A., & Dodin, A. V. 2017, AstL, 43, 344
Santos, N. C., Israelian, G., & Mayor, M. 2004, A&A, 415, 1153
Savel, A. B., Dressing, C. D., Hirsch, L. A., et al. 2020, AJ, 160, 287
Schlafly, E. F., & Finkbeiner, D. P. 2011, ApJ, 737, 103
Schlegel, D. J., Finkbeiner, D. P., & Davis, M. 1998, ApJ, 500, 525
Schwab, C., Rakich, A., Gong, Q., et al. 2016, Proc. SPIE, 9908, 99087H
Scott, N. J., & Howell, S. B. 2018, Proc. SPIE, 10701, 107010G
Scott, N. J., Howell, S. B., Gnilka, C. L., et al. 2021, FrASS, 8, 138
Sha, L., Huang, C. X., Shporer, A., et al. 2021, AJ, 161, 82
Shallue, C. J., & Vanderburg, A. 2018, AJ, 155, 94
Smith, J. C., Stumpe, M. C., Cleve, J. E. V., et al. 2012, PASP, 124, 1000
Stassun, K. G., Oelkers, R. J., Pepper, J., et al. 2018, AJ, 156, 102
Stassun, K. G., Oelkers, R. J., Paegert, M., et al. 2019, AJ, 158, 138
Stumpe, M. C., Smith, J. C., Catanzarite, J. H., et al. 2014, PASP, 126, 100
Stumpe, M. C., Smith, J. C., Cleve, J. E. V., et al. 2012, PASP, 124, 985
Teske, J. K., Wang, S., Wolfgang, A., et al. 2018, AJ, 155, 148
Thorngren, D. P., Fortney, J. J., Lopez, E. D., Berger, T. A., & Huber, D. 2021, ApJL, 909, L16
Tokovinin, A. 2018, PASP, 130, 035002
Tokovinin, A., & Cantarutti, R. 2008, PASP, 120, 170
Tokovinin, A., Fischer, D. A., Bonati, M., et al. 2013, PASP, 125, 1336
Torres, G., Konacki, M., Sasselov, D. D., & Jha, S. 2004, ApJ, 614, 979
Trifonov, T., Brahm, R., Espinoza, N., et al. 2021, AJ, 162, 283
Valenti, J. A., & Fischer, D. A. 2005, ApJS, 159, 141
Vanderburg, A., & Johnson, J. A. 2014, PASP, 126, 948
Virtanen, P., Gommers, R., Oliphant, T. E., et al. 2020, NatMe, 17, 261
Vogt, S. S., Allen, S. L., Bigelow, B. C., et al. 1994, Proc. SPIE, 2198, 362
Wes McKinney 2010, in Proc. 9th Python in Science Conf., ed. S. van der Walt & J. Millman, 56
Wheatley, P. J., West, R. G., Goad, M. R., et al. 2018, MNRAS, 475, 4476
Wittenmyer, R. A., Clark, J. T., Trifonov, T., et al. 2022, AJ, 163, 82
Wittenmyer, R. A., Horner, J., Carter, B. D., et al. 2018, arXiv:1806.09282
Wong, I., Shporer, A., Zhou, G., et al. 2021, AJ, 162, 256
Yee, S. W., Petigura, E. A., & von Braun, K. 2017, ApJ, 836, 77
Yee, S. W., Winn, J. N., & Hartman, J. D. 2021, AJ, 162, 240
Zhou, G., Huang, C. X., Bakos, G. Á., et al. 2019, AJ, 158, 141
Zhou, G., Quinn, S. N., Irwin, J., et al. 2020, AJ, 161, 2
Ziegler, C., Tokovinin, A., Briceño, C., et al. 2019, AJ, 159, 19
Ziegler, C., Tokovinin, A., Latiolais, M., et al. 2021, AJ, 162, 192